Exp. Theo. NANOTECHNOLOGY 10 (2026) 1519-1549 https://doi.org/10.56053/10.3.1519

Functionally graded coating (Cu/Zn/Sn) to improve steel bar performance using a modified spray technique: Experimental and simulation study

Sana S. Hameed[1], *Rana A. Anaee*[2,3,*], *Ahmed M. Al- Ghaban*[2]

[1]Ministry of Transport, Baghdad, Iraq
[2]College of Materials Eng., University of Technology- Iraq, Baghdad, Iraq
[3]Nanotechnology and Advanced Materials Researches Center, University of Technology- Iraq, Baghdad, Iraq
*) Email rana.a.majed@uotechnology.edu.iq

Received 11/4/2026, *Received in revised form* 12/5/2026, *Accepted* 22/6/2026, *Published* 15/7/2026

This study presents a novel functionally graded (FGCs) coating materials designed to improve the corrosion resistance of steel rebars embedded in concrete exposed to aggressive chloride environments. A triple-layered Cu/Zn/Sn coating at the nanoscale is applied using a modified spray coating technique that integrates manufacturing efficiency with metallurgical bonding. Reinforced concrete specimens are exposed to a 3.5 wt.% NaCl solution for 28, 56, and 90 days at three different temperatures (298, 308, and 318 K) to assess long-term corrosion performance under simulated marine conditions. Comprehensive surface characterization is performed using X-ray diffraction (XRD), scanning electron microscopy (SEM), energy dispersive spectroscopy (EDS), atomic force microscopy (AFM), and microhardness testing. The results confirmed the formation of a dense, well-adhered protective layer with improved surface uniformity. Electrochemical tests, including Tafel polarization and electrochemical impedance spectroscopy (EIS), demonstrated a substantial improvement in corrosion resistance. At 298 K after 28 days of immersion, the coated samples exhibited a corrosion current density of 0.299×10^{-7} A/cm² and achieved a maximum inhibition efficiency of 97.92%. Additionally, the porosity percentage is extremely low at 1.29×10^{-7}%. The EIS analysis supported these findings, revealing that the highest solution resistance is 21,521 Ω·cm². Furthermore, the coated steel exhibited enhanced mechanical properties, with surface hardness increasing from 195.8 HV (uncoated) to 221.4 HV. These results indicate that this FGM coating provides durable protection against chloride-induced corrosion, offering a practical and cost-effective solution for prolonging the life span and performance

of reinforced concrete structures exposed to marine and de-icing environments. Notably, these findings aligned well with DFT-based simulations, which confirmed the coating's thermal stability and chloride adsorption behavior at the atomic level.

Keywords: Copper; Tin, Zinc; Steel bar; FGCs.

1. INTRODUCTION

Surface coating is one of the most effective techniques for surface modification and material engineering. It involves applying a protective layer onto metal structures to enhance durability, corrosion resistance, and wear performance. By acting as a physical barrier between the substrate and the environment, coatings play a critical role in extending the service life of components, particularly under harsh or corrosive conditions. This function is especially important in construction, where concrete structures are often exposed to aggressive environmental factors [1,2]. Steel reinforcing bars (rebars), commonly used in reinforced concrete, are particularly vulnerable to corrosion due to exposure to moisture, chlorides, sulfates, and other aggressive agents. Corrosion of rebars can compromise the mechanical integrity of concrete structures, leading to safety hazards, costly repairs, and reduced structural longevity. To mitigate this, protective coatings are applied to rebar surfaces to inhibit the electrochemical reactions responsible for corrosion initiation and propagation. Addressing this challenge remains a key focus in the design and maintenance of reinforced concrete systems [3,4]. Coatings are generally categorized into two broad types: metallic and non-metallic. These differ significantly in composition, performance, and applications. Metallic coatings, typically composed of pure metals or alloys, are widely used to improve corrosion resistance, electrical conductivity, and surface hardness under mechanical loads [5-7]. In contrast, non-metallic coatings, which include inorganic materials (e.g., ceramics, oxides) and organic compounds (e.g., polymers, resins), are favored for their insulating properties, chemical stability, and barrier protection [8, 9]. The choice between these systems depends on the specific performance requirements of the application, including environmental conditions, mechanical stress, cost, and long-term reliability. For more demanding engineering environments, especially those involving aggressive chemical or electrochemical exposure, traditional coatings may fall short. In such cases, functionally graded materials (FGMs) offer a more advanced solution. FGMs are engineered with a gradual transition in composition and structure across the material volume, allowing tailored performance and improved resistance to failure under complex service conditions [10,11]. Unlike conventional single or bilayer systems, which are prone to cracking or delamination due to thermal mismatch or low fracture toughness, FGMs provide smooth property gradients that mitigate such risks. A notable application of FGMs in corrosion protection is functionally graded coatings (FGCs). These coatings exhibit continuous compositional transitions that reduce thermal stresses, enhance mechanical toughness, and improve bonding at the coating–substrate interface [12,13]. FGCs often consist of carefully distributed ceramic and metallic phases, which enhance chemical resistance and structural integrity. The presence of intermediate layers within the gradient structure reinforces adhesion and reduces delamination under mechanical loads.

Furthermore, a uniform phase distribution helps suppress crack initiation and growth [14, 15]. Advanced fabrication methods such as thermal spraying enable precise control over these gradients, allowing coatings to deliver localized, application-specific performance. In high-temperature environments, incorporating metallic phases enhances thermal stability and prolongs service life. Notably, recent studies have shown that even relatively thin FGCs can achieve fracture resistance comparable to that of significantly thicker conventional coatings [16, 17]. Several recent studies have investigated the development, performance, and optimization of surface coatings, particularly

functionally graded systems for corrosion protection, offering valuable insights into their structural design, fabrication methods, and long-term behavior under aggressive service conditions. In 2016, M. H. Allahyarzadeh et al. developed eight-layer functionally graded nickel-tungsten coatings on steel substrate via pulse electrodeposition. The coatings showed good corrosion resistance, with no crack propagation to the substrate, and superior wear resistance compared to pure Ni [18], in 2018, Jarnail Singh et al. investigated functionally graded hydroxyapatite coatings on Ti6Al4V alloy deposited by plasma spraying. The coatings adhered well without interfacial cracks, and heat treatment improved the corrosion resistance, indicating extended service life [19], on the other hand, Ameen Uddin Ammar et al. coated cast iron samples with PVA/PANI/FLG and TiO_2/GO nanocomposites using dip-coating. In seawater, PVA/PANI/FLG reduced the corrosion rate by 52%, while TiO_2/GO achieved a 94% reduction. Porosity and coating capacitance significantly influenced these results [20], in 2019, Sistika Banthia et al. studied the performance of copper-based functionally graded coatings under marine conditions and varying wear loads. The Cu/Cu–SiC FGC exhibited higher corrosion resistance than the Cu FGC and showed superior wear resistance under high loads [21], in 2023, Norhan Ashraf Ismail et al. applied smart multilayered epoxy coatings for steel corrosion protection. Zn/Al-LDH with DOD and UFMCs with LA are incorporated into the epoxy matrix. Results showed that the double-layer coating (DL-EP) outperformed the single-layer (LDH-EP) due to efficient release of active agents [22], in 2024, Prabhat Ranjan et al. improved the wear resistance of cast steel cylinder liners by applying five-layer FGM coatings using the HVOF Technique. Employed C1 (WC-10Co-4Cr), C2 (WC-12Co), and C3 (Ni-25Cr) powders to fabricate the coatings. Reported that FGCS-1 exhibited the lowest wear compared to FGCS-2 and FGCS-3 [23], M. Sathish et al. deposited three layers TiC–12Co–10ZrO_2/NiCoCrAlMo FGC on SS410 substrates via APS technique. The results revealed that by optimizing ceramic proportions. The FGC showed significantly higher microhardness and lower wear rate than the uncoated samples [24], and Marquardt et al. [25] demonstrated FGM fabrication from duplex steel to Co-Cr alloy via powder-based directed energy deposition. Achieved smooth material transitions with low porosity; outer cracks are likely due to thermal gradients, and the microhardness remained stable. This study aims to apply multiply layers of metallic nanoparticles as coatings known as functionally graded coatings (FGCs) using a novel method during the manufacturing of steel reinforcing bars, referred to as “Modified Spray Coating” technique. The primary objective is to simulate the temperature of the hot-rolling process to provide an economical and efficient approach, compared to conventional methods, by simultaneously manufacturing and coating steel rebars, [26, 27]. During this process, the properties of the substrate are integrated with those of the metallic coating, thereby producing a composite material with enhanced mechanical properties and good corrosion resistance [28,29].

2. EXPERIMENTAL

2.1 Materials

Steel reinforcing bars with the dimensions of 13 cm in length and 1.2 cm in diameter are used as rebar samples in the concrete mixture. Their chemical composition is shown in Table 1, in accordance with ISO-6935-2 [30]. As for coating, three different metal powders (copper, zinc, and tin), produced by Central Drug House (P) Ltd., Thomas Baker (Chemicals) Pvt. Ltd., and Sigma-Aldrich, respectively, with particle sizes ranging from 20 to 250 nm and purity varying between 99.5% and 99.6%, are used to coat the steel rebar samples.

Table 1 Percentage composition of elements in steel rebar.

C	Si	Mn	P	S	Cr	Ni	Cu	Al
0.22	0.6	1.6	0.05	0.05	0.1	0.1	0.33	0.01

In this work, the preparation of all concrete samples involved the use of Sulphate Resisting Portland Cement (SRPC) from the Lafarge-cement factory. The chemical composition and main compounds of SRPC are presented in Table 2. In addition, sand containing 0.4% So_3, along with 10 mm maximum size black-crushed gravel is used as fine and coarse aggregates, respectively [31, 32].

Table 2 Chemical properties of SPRC.

Chemical Composition	Chemical Formula	Test Result %	Iraqi Standard limits No.5/2019
Lime	CaO	63.6	-
Silica	SiO_2	19.35	-
Alumina	Al_2O_3	3.98	-
Iron Oxide	Fe_2O_3	5.03	-
Sulfate	SO_3	1.71	≤ 2.5 If $C_3A < 5$
Magnesium oxide	MgO	3.32	≤ 5
Chlorine content	Cl	0.02	≤ 0.1
Insoluble Residue	I.R	1.1	≤ 1.5
Loss on Ignition	L.O.I	3.05	≤ 4
Tri-Calcium Silicate	C_3S	72.99	-
Di-Calcium Silicate	C_2S	0.4	-
Tri-Calcium Aluminate	C_3A	2.05	-
Tetra Calcium Aluminoferrite	C_4AF	15.31	-

The concrete mixture is prepared by dry mixing cement, sand, and gravel in an electric pan mixer with a 50L capacity for two minutes to achieve even dispersion. Water is then gradually added while mixing proceeded for another three minutes until a homogeneous mixture is achieved. Table 3, provides the required amounts of concrete mix.

Table 3 The concrete mix quantities.

Cement (Kg/m^3)	Sand (Kg/m^3)	Gravel (Kg/m^3)	Water (L/m^3)
310	720	1190	154.5

Steel rebars are installed vertically inside cube-shaped molds, each measuring 10 × 10 × 10 cm, as shown in Figure 1. Subsequently a concrete mixture is poured into these molds, which are then subjected to vibration for approximately one minute to facilitate the removal of air bubbles and ensure adequate compaction. After 48 hours of casting, the molds are opened, and the concrete samples are carefully extracted and submerged in tap-water for 28 days to complete the curing process. Next, all reinforced concrete samples are immersed up to 5 mm below their top surfaces in a seawater solution containing 3.5 wt.% NaCl for three different durations (28, 56, and 90 days) to assess the corrosion resistance of the samples both before and after the application of protective coatings.

Figure 1 Concrete molds before and after casting.

2.2 Coating process

This study introduces a novel coating methodology (referred to as modified spray coating technique), which integrates the manufacturing and coating of steel rebar to enhance efficiency and reduce costs. This method simulates the temperature of the hot-rolling process by employing a cylindrical induction furnace, as illustrated in Figure 2. The furnace is enclosed by two stainless steel discs: one disc holds the steel rebar to be coated and a temperature sensor, while the other disc features nozzles positioned both above and below the steel reinforcing bar. Metal powder (20–250 nm in size) is sprayed through these nozzles at a pressure of 116 bar, forming a functionally graded coating (FGC) with sequential layers of copper, zinc, and tin (Cu/Zn/Sn). These layers are arranged based on their melting points, from highest to lowest: copper (1000–1050°C), zinc (400–440°C), and tin (200–220°C). The rebar is preheated to the respective temperatures before each powder is applied, ensuring that when the sprayed powder hits the hot rebar, it melts and forms a smooth, protective coating over the entire steel surface.

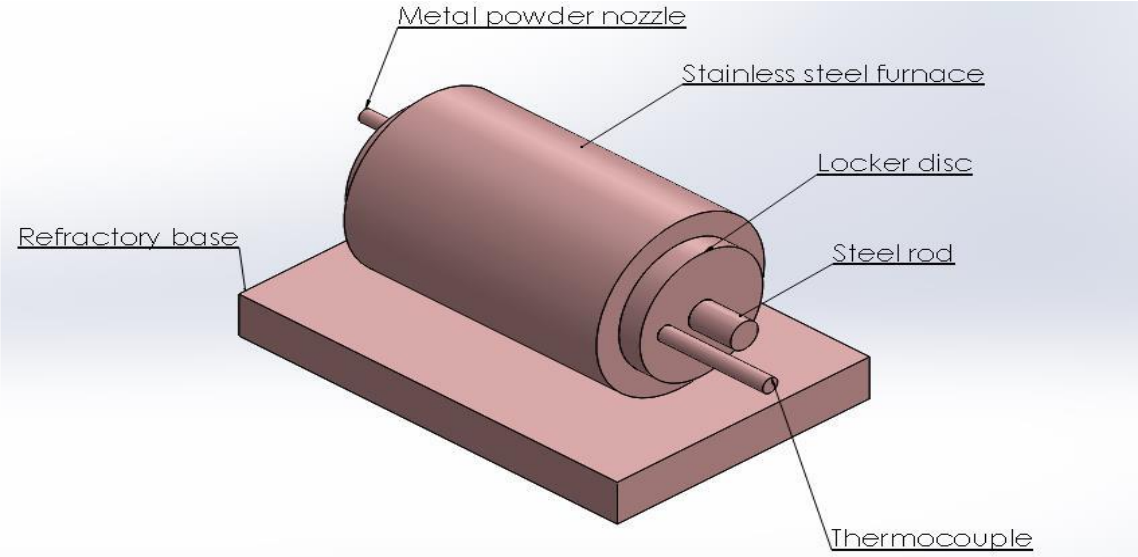

Figure 2 Detailed layout of the cylindrical induction furnace design.

Afterward, the coated rebar is bent to a 90° angle (see Figure 3.) to evaluate the coating's durability and adhesion under deformation, simulating mechanical stresses encountered in real-world applications. Following bending, samples are visually examined for cracks, peeling, or flaking. The coating remained intact and well-adhered to the substrate [33].

Figure 3 Coated sample during the bending process.

2.3 Measurements

The formed phases are analyzed at room temperature by X-ray diffraction (XRD) using a Shimadzu 6000. The analysis is performed at a scanning speed of 5°/min and an angular range varying from 10° to 90°, using the wavelength of Kα radiation (λ = 0.154065 nm) with 40 kV and a power supply of 30 mA. The morphological examination is conducted using a scanning electron microscope (SEM) (FEI Inspect™ F50, Thermo Fisher Scientific) after applying an accelerating voltage of 30 kV and an electric current of 170 µA. Additionally, the elemental composition is analyzed using energy-dispersive spectroscopy (EDS) with an Axia ChemiSEM device from Thermo Fisher Scientific. The atomic force microscope (AFM) is employed to examine the topography of the sample by measuring its surface roughness and particle size. This is performed using a FlexAFM-Axiom device equipped with a C3000 controller (90–240 V), manufactured by Nanosurf AG. On the other hand, the microhardness measurements are recorded using a digital-microhardness tester (HMV-2) manufactured by Shimadzu company /Kyoto, Japan.

2.4 Corrosion

The electrochemical properties are measured by using an electrochemical cell consisting of three electrodes: (1) The working electrode (WE), which includes the coated and uncoated steel-rebar samples; (2) The reference electrode (RE), which is a saturated calomel electrode (SCE); (3) An

auxiliary/counter electrode made of platinum, positioned directly opposite the (WE) in the electrochemical cell. All tests are conducted at different temperatures (25, 35, 45 °C) using (Potentiostat, model: CS350M) from Corrtest, as shown in Figure 4. The Tafel polarization test consisted of two steps: First, the open circuit potential (OCP) is measured by immersing the samples in a saline solution containing 35 g/L of sodium chloride for approximately 15 min and recording the potentials applied to (R.E.). Then, potentials of (± 200 mV) around the (OCP) are applied at a scan rate of (1mV/sec) to collect data on corrosion parameters such as corrosion current density (i_{corr}), corrosion potential (E_{corr}), and Tafel slops (b_a and b_c) which are used in further calculations [34-37]. As for the electrochemical impedance spectroscopy (EIS), it is determined for all steel samples by recording Nyquist plots to measure the charge transfer resistance, solution resistance, and diffusion process.

Figure 4 The electrochemical cell used for corrosion resistance measurement.

3. RESULTS AND DISCUSSION

3.1. Characterization of coated surface

XRD test is used to characterize the surface of both coated and uncoated steel samples. The main peaks of steel rebar can be observed in Figure5a, including those at 2θ values of 43.76°, 59.84°, 64.28° and 81.68° , which correspond to the steel reference pattern according to JCPDS card No. 35-1375. On the other hand, the XRD pattern of the steel bar coated with three layers (Cu/Zn/Sn), arranged from bottom to top is shown in Figure5b. This Pattern exhibits multiple peaks compared to that of plain rebar. The peaks corresponding to the deposition of individual metals are relatively weak. However, copper diffusion from the bottom layer to the tin top layer through the intermediate zinc layer is observed, likely due to the migration of Cu-atoms along grain boundaries and their precipitation out. This diffusion resulted in the formation of the Cu_6Sn_5 intermetallic phase, as confirmed by comparison with JCPDS card No. 45-1488 [38,39].

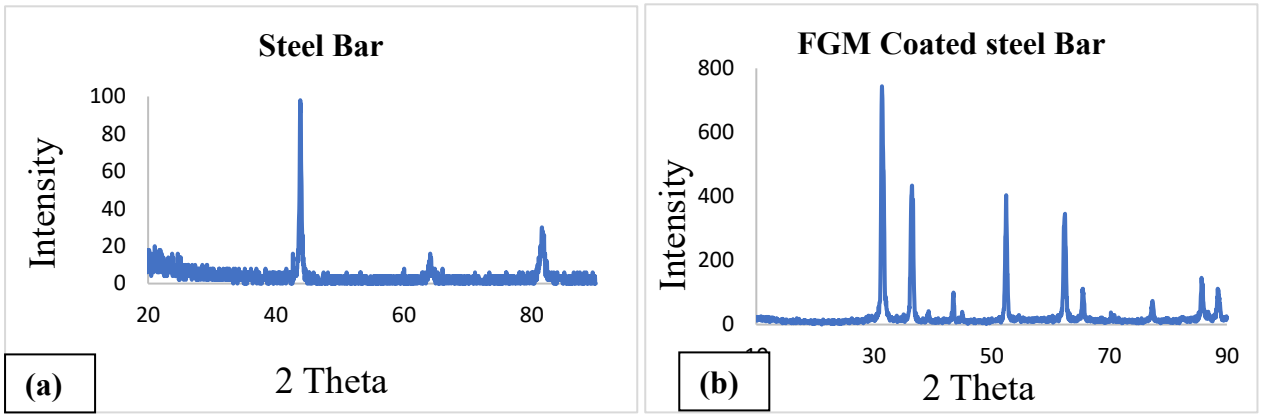

Figure 5 XRD analysis of (a) steel bar and (b) FGM coated steel.

The surface morphology of the plain and FGM-coated steel bars is examined by the Scanning electron microscopy (SEM). Figure 6a, displays SEM images of the uncoated steel sample, revealing irregular edges associated with the structural features of steel bars used in construction. These irregularities enhance adhesion with cement paste, resulting in a rough surface, Figure 6b presents the SEM images of the FGM coated surface, illustrating the formation of a compact as bronze layer, as conformed by XRD analysis. This observation aligns with reference [40], which describes a harmonic-structure containing a network of bronze with a fine dendritic structure.

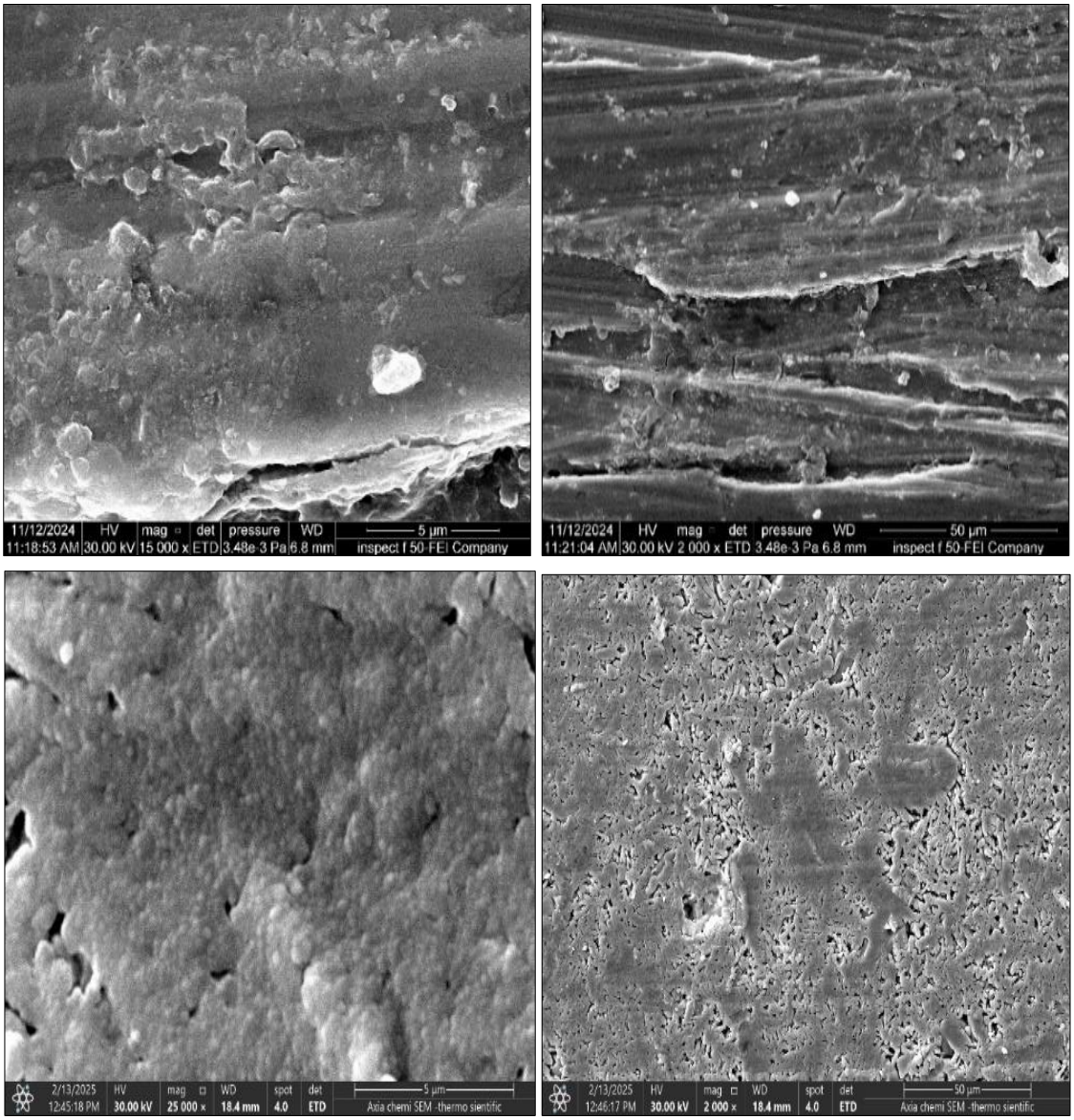

Figure 6 SEM micrograghs of (a) uncoated-steel and (b) FGM-coated steel.

The energy dispersive spectroscopy (EDS) analysis of the uncoated steel bar, presented in Figure 7a, showed the elemental composition and verified the existence of all base elements, particularly iron 86.7 wt% as the primary constituent. In contrast, The EDS-analysis of the FGM coated sample in Figure 7b, revealed that the weight percentages of of copper, tin, and zinc are 29.5%, 10.6%, and 33.4 respectively, respectively, along with 6.8% oxygen, and 0.3% Ni.

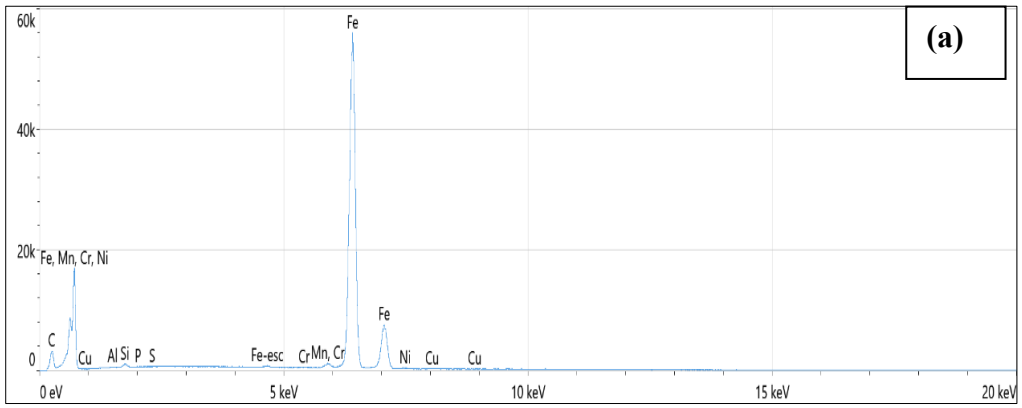

Element	Weight %
Al	0.1
Si	0.5
Mn	1.3
Fe	**86.7**
Ni	0.3
Cu	0.2
Cr	0.1

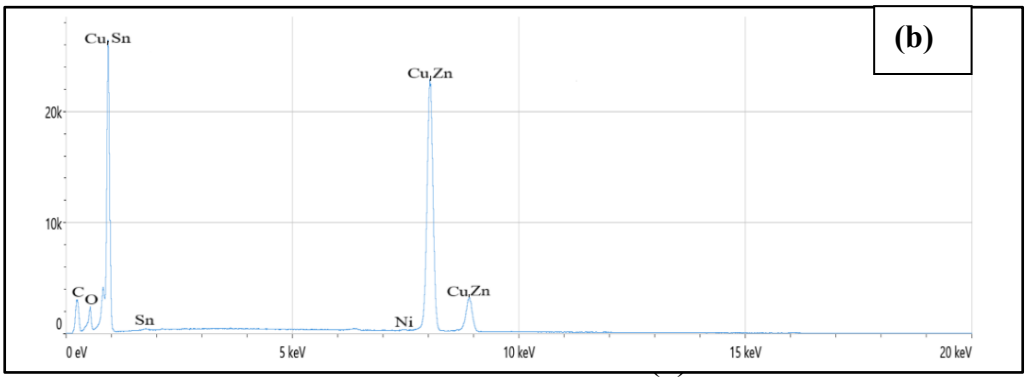

Element	Weight %
O	6.8
Ni	0.3
Sn	10.6
Cu	29.5
Zn	33.4

Figure 7 Elemental composition of: (a) uncoated steel and (b) FGM-coated steel.

Atomic force microscopy (AFM) is used to investigate the surface topography of the plain steel rebar and FGM-coated steel, as illustrated in Figures. (8 and 9). The observations in Figure 8 included both two-dimensional and three-dimensional representations, emphasizing the valley-like surface features. These surface characteristics play a critical role in enhancing the bonding efficiency between the steel rebar and the cement paste, contributing to a high surface roughness of 133.6 nm, In contrast, the AFM scan of the functionally graded coatings (FGCs) on the steel surface, revealed a structure similar to a carpet, with a more uniformly incorporated dispersion layer achieving the lowest roughness (11.60 nm). This confirms the incorporation of the three metals in the coating, from the first deposited layer (bottom) to the third deposited layer (top), as shown in Figure 9.

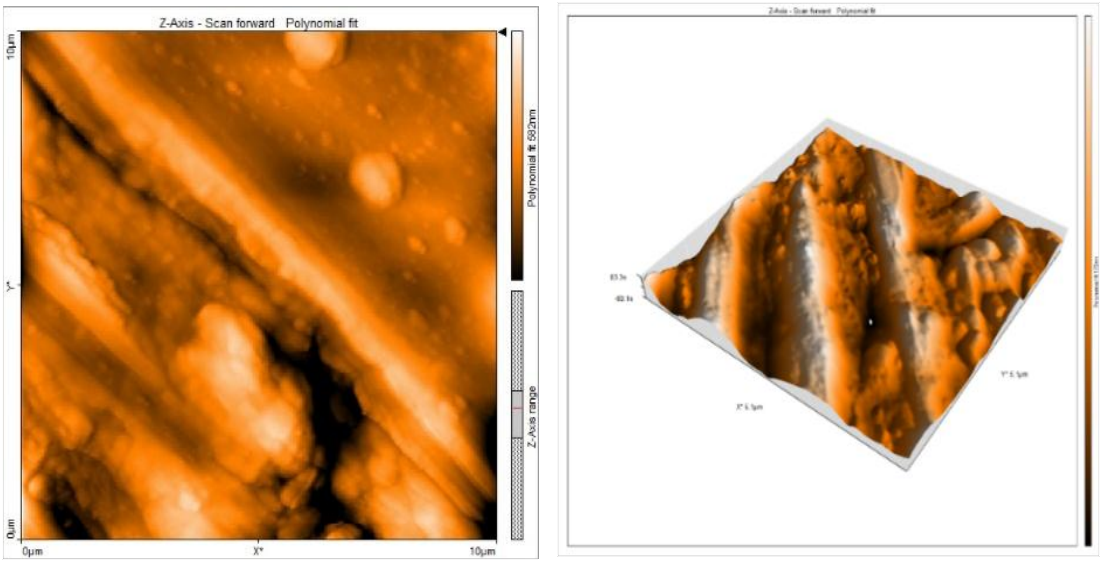

Figure 8 AFM of steel rebar.

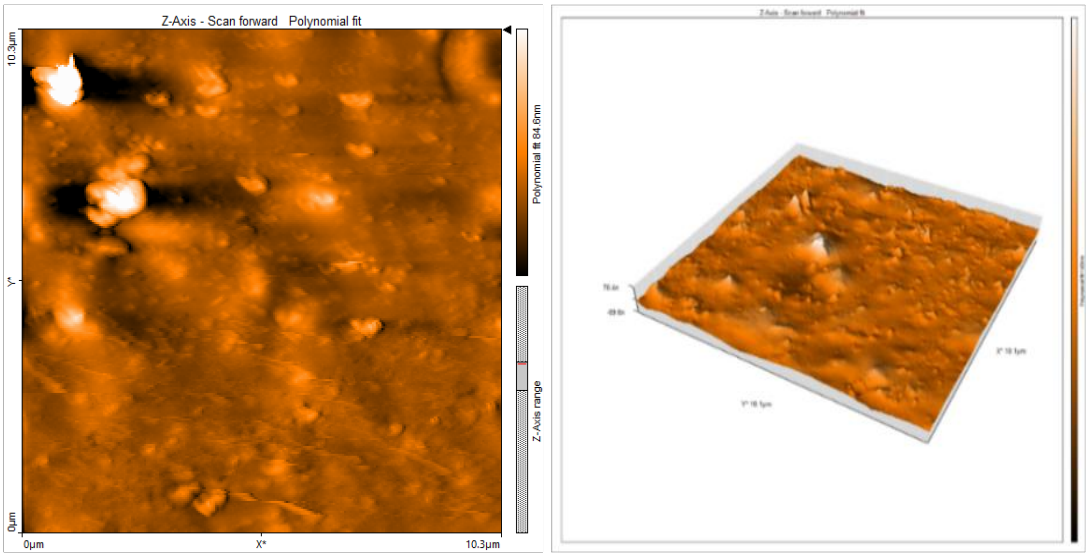

Figure 9 AFM analysis of FGCs on steel bar.

The particle distribution chart of the plain steel bar sample is presented in Figure 10a, showing that the region with the highest concentration of large particles has a mean diameter of (195.7 nm), while in Figure 10b, a regular distribution is obtained for the particles in the FGC materials on steel sample, with a mean diameter of (93.06 nm).

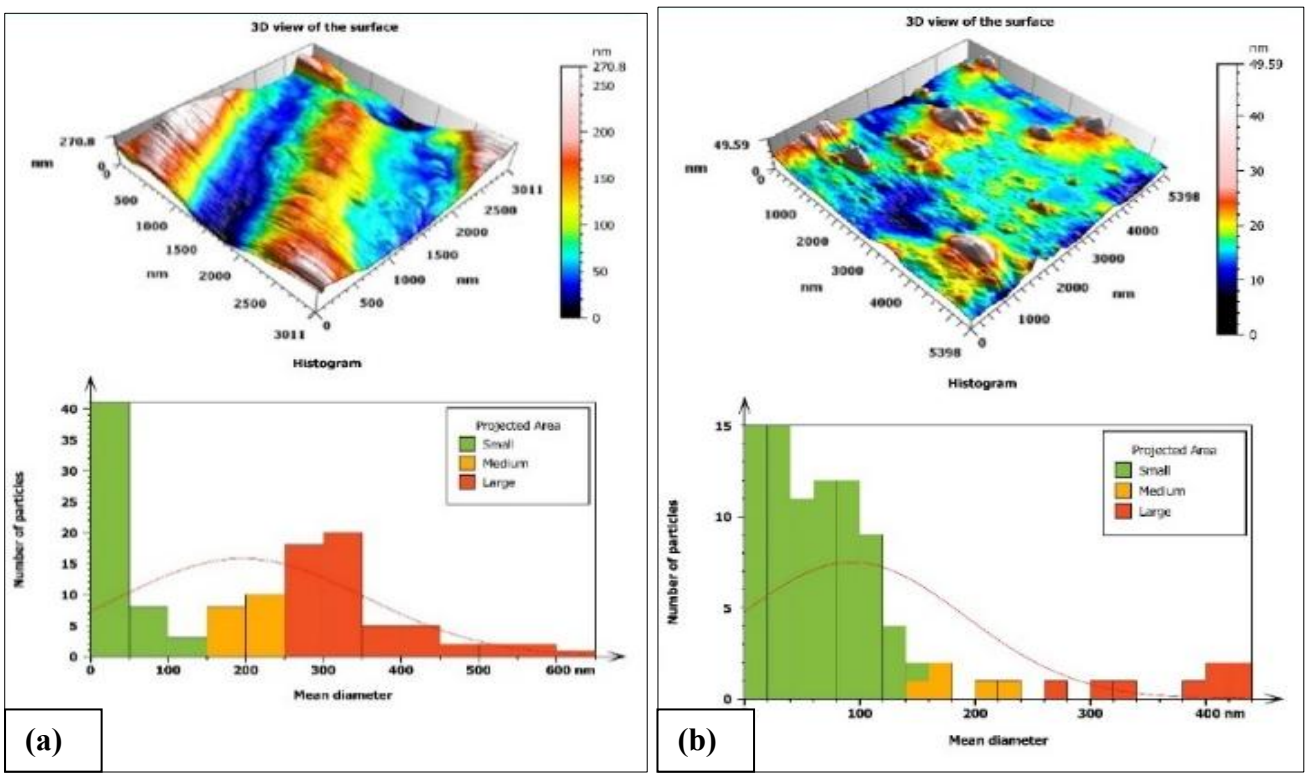

Figure 10 Particles distribution-chart of (a) plain steel and (b) FGCs on steel rebar.

3.2. Hardness

Microhardness is measured by taking the average of three readings. The plain (uncoated) steel bar surface recorded an average value of 195.8 HV, while the FGM coated layer reached a mean value of 221.4 HV. This increase in microhardness is attributed to the functionally graded coating's unique triple-layer structure, which results in a progressive hardness enhancement with increasing coating thickness [41].

3.3. Corrosion behavior

This research aims to reduce corrosion susceptibility, as assessed through the analysis of polarization curves. Tafel plots for plain and coated steel rebars following immersion durations of 28, 56, and 90 days are presented in Figures 11 to 13. Overall, the corrosion potential demonstrates time-dependent variation, while the corrosion current exhibits increasing trend over prolonged exposure periods. This behavior is likely attributed to the extended interaction with aggressive ions that penetrate the cementations matrix, eventually compromising the passive layer on the steel surface through chemical degradation [42].

The anodic reaction produces ferrous cations [43, 44]:

$$Fe \rightarrow Fe^{2+} + 2e \quad (1)$$

While the hydroxyl ions are the result of the cathodic reaction.

$$1/2O_2 + 2e + H_2O \rightarrow 2OH^- \quad (2)$$

Ferrous hydroxide forms through the reaction between (Fe^{2+}) and (OH^-) ions, and is subsequently oxidized to ferric hydroxide upon exposure to atmospheric oxygen in the presence of water.

$$Fe^{2+} + 2OH^- \rightarrow Fe(OH)_2 \quad (3)$$

$$4Fe(OH)_2 + 2H_2O + O_2 \rightarrow 4Fe(OH)_3 \quad (4)$$

When the latter undergoes dehydration, it forms hydrated ferric oxide over time:

$$2Fe(OH)_3 \rightarrow Fe_2O_3.H_2O + 2H_2O \quad (5)$$

Hydrated ferric oxide is highly porous, so when the chloride ion concentration increases, the passive layer on the steel surface is locally disrupted, leading to the formation of pitting corrosion. The area attacked by chloride ions acts as an anode, while the surrounding passivated surface serves as a cathode. In the anodic region, iron (II) ions react with Cl^-ions to form ferrous chloride, which subsequently hydrolyzes in water to produce ferrous hydroxide and hydrochloric acid, further accelerating the corrosion process.

$$Fe^{2+} + 2Cl^- \rightarrow FeCl_2 \quad (6)$$

$$FeCl_2 + 2H_2O \rightarrow Fe(OH)_2 + 2HCl \quad (7)$$

The mechanism described above is self-generative, and once it starts, it continues, as the initiation of a pit creates a localized environment that promotes its own growth. This process is autocatalytic, as the breakdown of the passive film by chloride ions enhances localizes acidity and chloride concentration. This continuous cycle accelerates metal dissolution and sustains the corrosion process over time [45].

The slopes of Tafel (b_c & b_a) and the corrosion current density (i_{corr}), can be utilized in the calculation of polarization resistance (R_P) according to the formula below [46]:

$$R_p = \frac{b_c \times b_a}{2.303 \times i_{corr}\,(b_c + b_a)} \quad (8)$$

Applying triple layers of metallic coatings (FGM) on the surface of steel rebars utilizing the "Modified Spray Coating Technique" can improve their resistance in harsh environments by preventing or minimizing the penetration of aggressive ions, and hence prolong the service life of concrete structures [47]. The data obtained from polarization measurements, as demonstrated in Tables 4 to 6, reveal a positive shift in corrosion potential and a notable reduction in corrosion current density. The protection efficiency (PE%) is correspondingly improved and is calculated based on the corrosion current densities of both coated and uncoated samples using the following equation [48, 49].

$$PE\ (\%) = \left[1 - \frac{i_{coated\ steel}}{i_{uncoated\ steel}}\right] \times 100 \quad (9)$$

The best efficiencies and resistances are recorded for steel bars coated with FGM, which resulted from the interaction of three layers within a single structure, exhibiting surface characteristics similar to bronze (Cu-Sn alloy). The data of protection efficiency at a constant immersion time showed that the best performance of the FGM coating is achieved at 298 K after 28 days of immersion, followed by 308 and 318 K after 56 days of immersion. The protective role of FGM is due to the formation of copper (Cu) and tin (Sn) oxides or hydroxides, as well as basic cupric chlorides and copper sulfates, as follows:

$$Sn + 2H_2O \rightarrow SnO_2 + 4H^+ + 4e \quad (10)$$

$$Cu + 2H_2O \rightarrow CuO_2 + 4H^+ + 4e \quad (11)$$

$$Cu + Cl^- \rightarrow CuCl + e \quad (12)$$

$$Cu + 2Cl^- \rightarrow CuCl_2 + 2e \quad (13)$$

$$Cu_2O + Cl^- + 2H_2O \rightarrow Cu_2(OH)_3Cl + H^+ + e \quad (14)$$

$$4Cu + SO_4^{2-} + 6H_2O \rightarrow CuSO_4.3Cu(OH)_2 + 6H^+ + 8e \quad (15)$$

$$4CuO + SO_4^{2-} + 2H_2O + 2H^+ \rightarrow CuSO_4.3Cu(OH)_2 \quad (16)$$

The protection with this coating is due to the formation of a protective film, which mainly included Cu_2O and $Sn(OH)_2$. Also, Sn atoms had the ability to separate the Cu_2O, which led to a decrease in ionic properties and improved the resistivity of the protective layer's barrier capability [50].

The the total coating porosity percentage (P%) is calculated based on the polarization resistance (R_p) of both the bare (substrate) and coated steel, the corrosion potential difference(ΔE), between them, and the anodic Tafel slope (b_a) of the substrate, as shown in the following equation [51]:

$$P(\%) = \left[\frac{R_p \text{ bare steel}}{R_p \text{ coated steel}}\right] \times 10^{(\frac{\Delta E}{ba})} \times 100 \quad (17)$$

The data in Table 7 confirmed the effectiveness of the FGM coating in providing a highly compact and defect-resistant barrier, significantly reducing the penetration of corrosive ions across all immersion durations and temperatures.

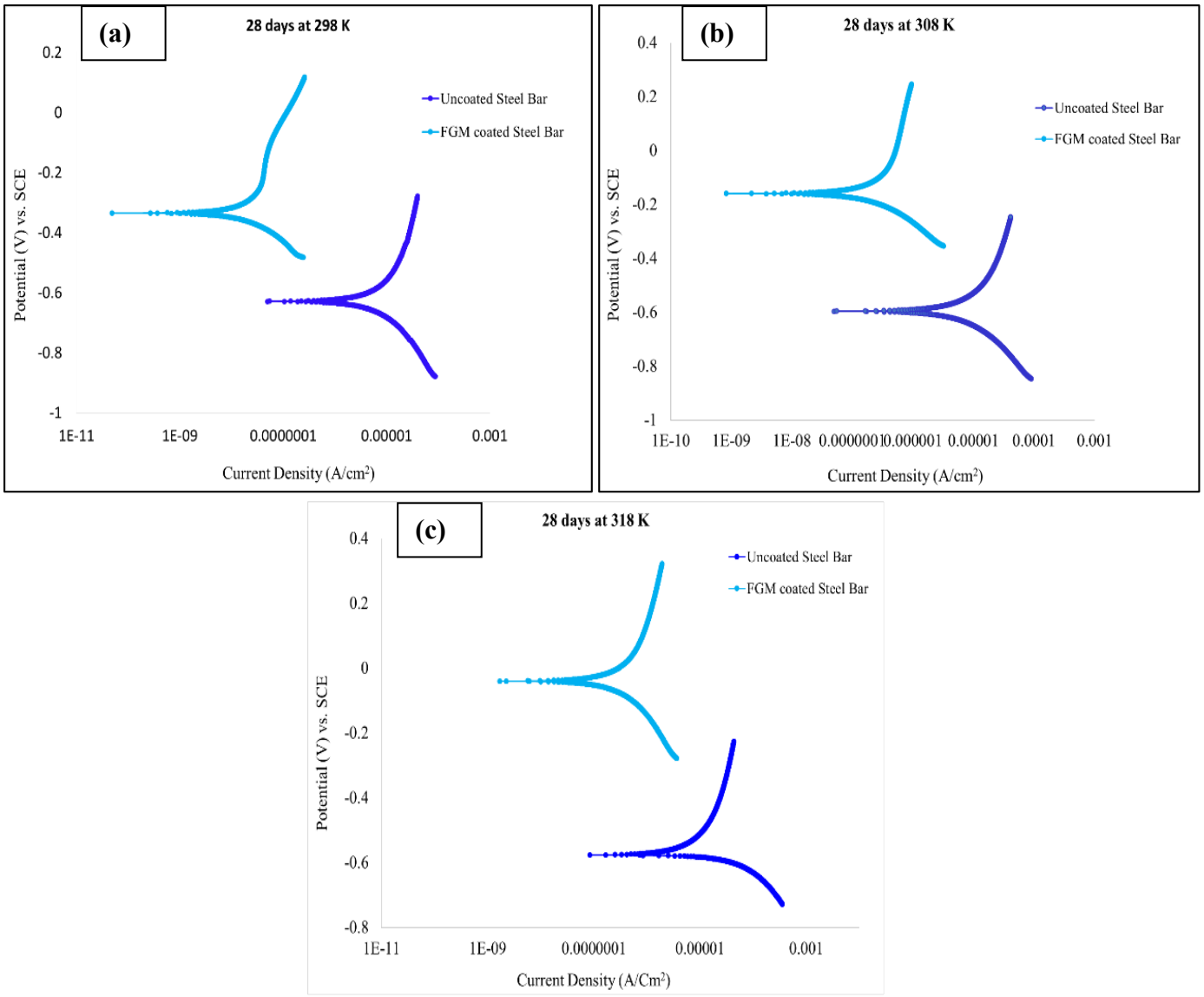

Figure 11 Tafel plots obtained after 28 days of immersion at three temperatures.

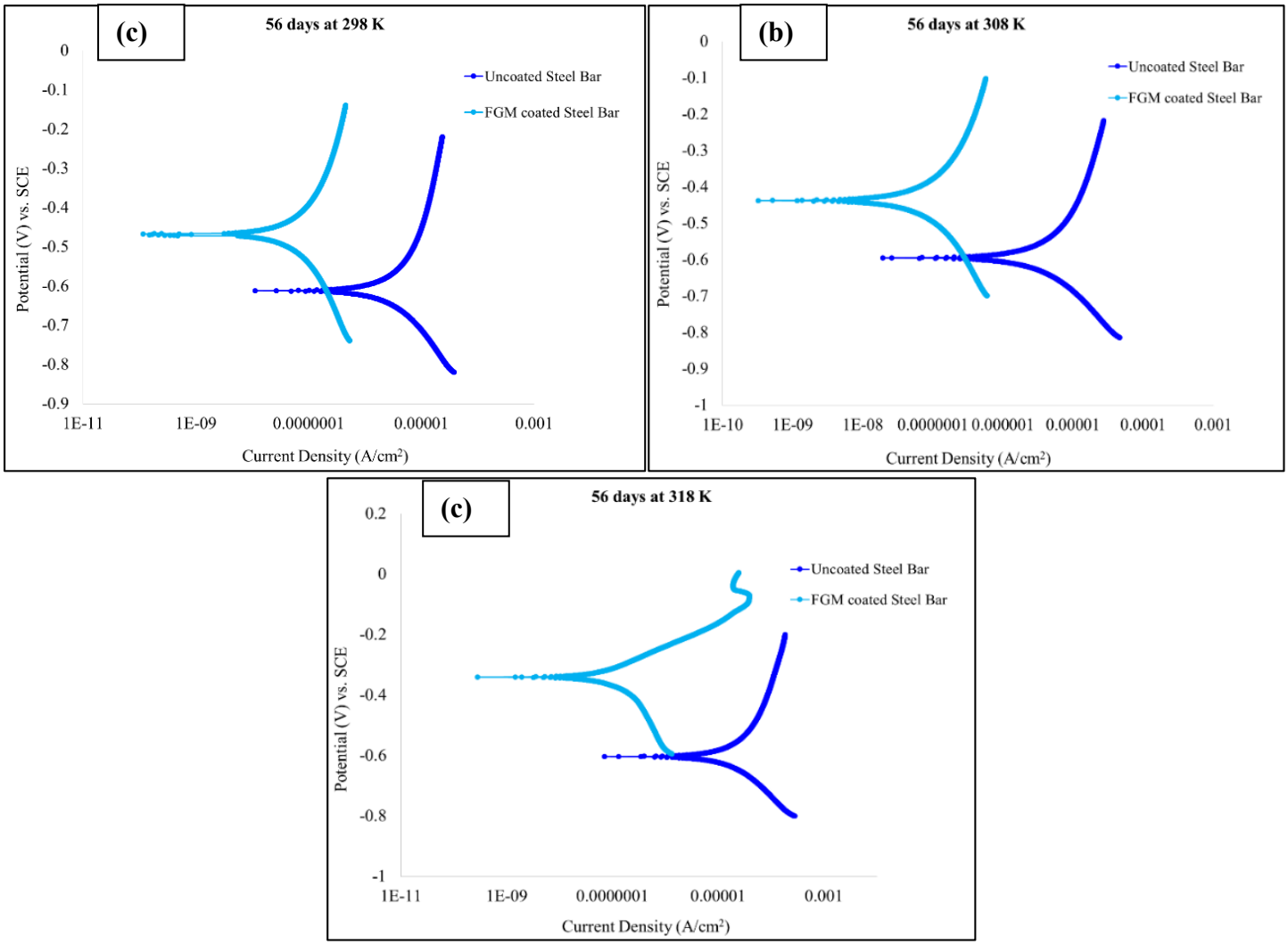

Figure 12 Tafel analysis after 56-day immersion period at varying temperatures.

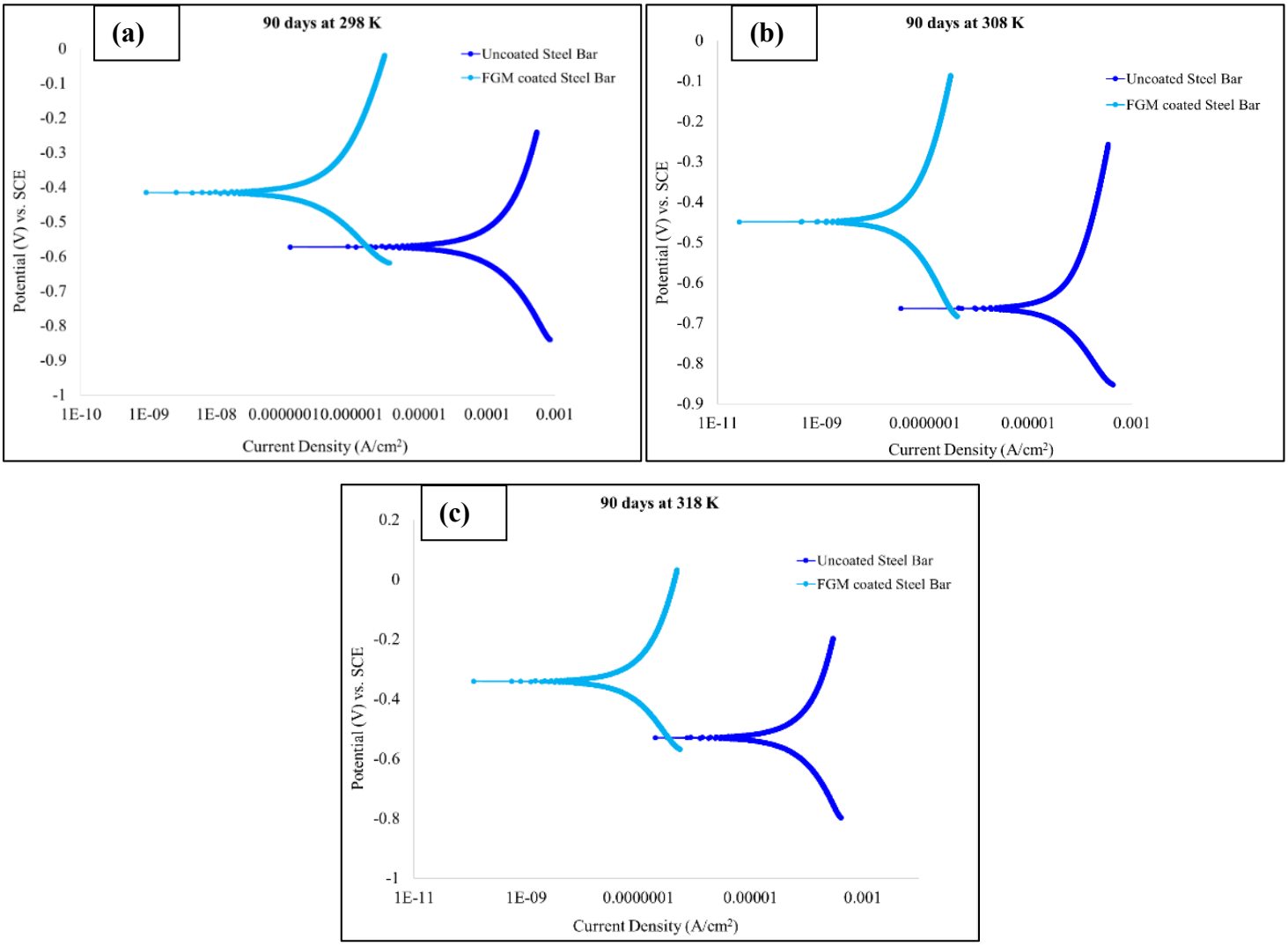

Figure 13 Tafel cutves after immersion time of 90 days at three different temperatures.

Table 4 Corrosion data for uncoated and coated steel bar after immersion time of 28 days at different temperatures.

Coating type	Temp. (K)	$-E_{corr}$ (V)	$i_{corr}x10^{-7}$ ($A.cm^{-2}$)	$-b_c$ ($mV.dec^{-1}$)	$+b_a$ ($mV.dec^{-1}$)	IE (%)	$R_p\times 10^{+4}$ ($\Omega.cm^2$)
Uncoated	298	0.628	14.4	40.727	39.864	-	0.608
	308	0.595	16.26	41.71	21.4	-	0.378
	318	0.576	18.415	37.92	25.58	-	0.360
FGM	298	0.335	0.299	25.207	34.32	97.92	21.132
	308	0.159	1.7817	53.224	71.654	89.04	7.452
	318	0.394	2.9732	50.698	67.653	83.85	4.237

Table 5 Corrosion data for uncoated and coated steel bar after immersion time of 56 days at different temperatures.

Coating type	Temp. (K)	$-E_{corr}$ (V)	$i_{corr}x10^{-7}$ ($A.cm^{-2}$)	$-b_c$ ($mV.dec^{-1}$)	$+b_a$ ($mV.dec^{-1}$)	IE (%)	$R_p\times 10^{+4}$ ($\Omega.cm^2$)
Uncoated	298	0.612	15.154	297.92	727.42	-	0.606
	308	0.595	16.682	31.04	38.399	-	0.447
	318	0.604	17.5263	31.622	36.34	-	0.419
FGM	298	0.523	1.023	33.058	37.905	93.24	7.504
	308	0.483	1.319	37.208	38.409	92.09	6.229
	318	0.340	1.827	50.643	53.884	89.57	6.212

Table 6 Corrosion data for uncoated and coated steel bar after immersion time of 90 days at different temperatures.

Coating type	Temp. (K)	$-E_{corr}$ (V)	$i_{corr}x10^{-7}$ ($A.cm^{-2}$)	$-b_c$ ($mV.dec^{-1}$)	$+b_a$ ($mV.dec^{-1}$)	IE (%)	$R_p\times 10^{+4}$ ($\Omega.cm^2$)
Uncoated	298	0.572	17.8285	36.612	49.27	-	0.512
	308	0.664	18.716	276.93	604.79	-	0.441
	318	0.529	19.2937	52.414	59.685	-	0.628
FGM	298	0.415	6.1741	305.29	547.27	65.36	13.800
	308	0.449	7.604	335.51	564.92	59.37	12.035
	318	0.340	8.0581	236.88	236.163	58.23	6.380

Table 7 Porosity percentages of FGM coatings at different immersion days and temperatures.

Temp. (K)	P%		
	28 days	56 days	90 days
298	1.29×10^{-7}	6.098	2.42×10^{-3}
308	2.15×10^{-20}	8.68×10^{-3}	1.61
318	6.54×10^{-7}	3.69×10^{-7}	6.7×10^{-3}

The electrochemical behavior of the metal-solution interface is examined using Electrochemical Impedance Spectroscopy (EIS), a technique employed to assess the corrosion resistance of the FGM coating by generating impedance spectra typically represented as semicircular Nyquist plots. In this research, the EIS measurements are conducted on specimens immersed for 28 and 56 days at 298 K. Figure 14 displays the Nyquist plots for uncoated and FGM-coated steel bars after 28 days of immersion at 298 K. The plots exhibit the well-known semicircle shape, revealing the presence of solution resistance (R_s), double-layer capacitance (C_{dl}), charge transfer resistance (R_{ct}), and Warburg impedance (Z_w). As the diameter of the semicircle increases, the charge transfer resistance (R_{ct}) also increases, with the FGM coated sample showing a larger diameter than the uncoated one. Detailed values are provided in Table 8. The FGM coating demonstrated the highest resistance values for both solution and charge transfer components, consistent with its superior performance in the Tafel polarization test. A comparable trend is noticed for samples immersed for 56 days at 298 K, where coated sample showed significantly greater resistance compared to the plain (uncoated) one. Due to

this pronounced difference, the uncoated data could not be included in the same plot (see Figure 15). The corresponding results are summarized in Table 9.

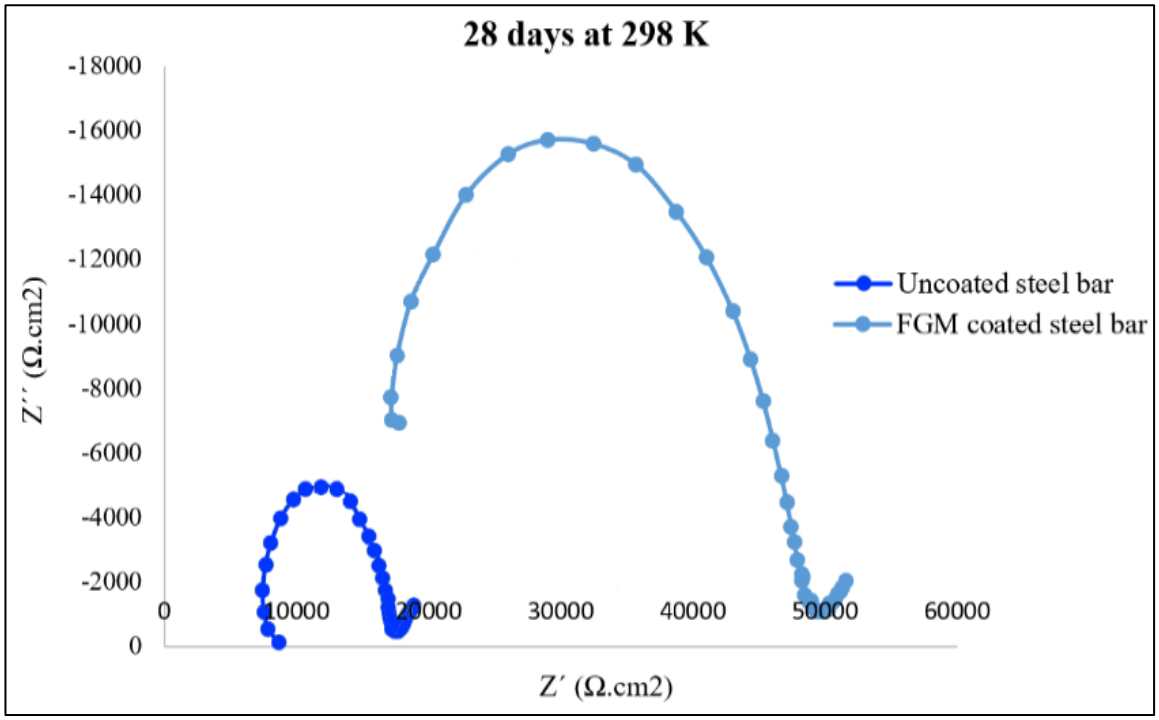

Figure 14 Nyquist plots after 28 days of immersion at 298K.

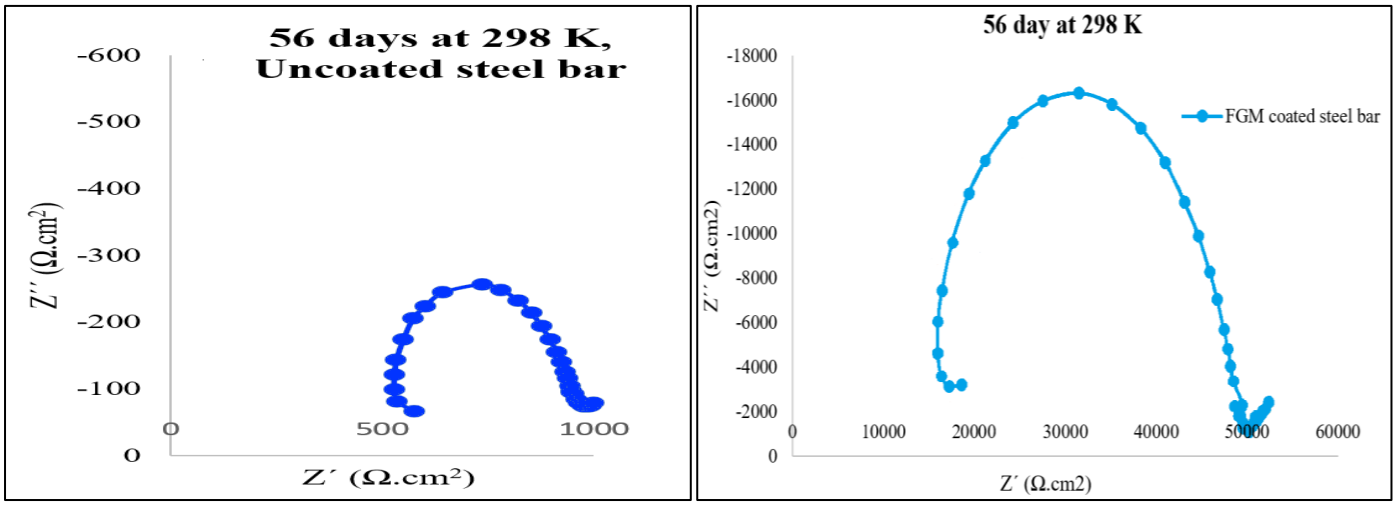

Figure 15 Nyquist plots following 56-days of exposure at 298K.

Table 8 EIS measured values after 28 days of immersion at 298 K.

Specimen	R_s (Ω.cm^2)	$R_s + R_{ct}$ (Ω.cm^2)	Z_w (Ω.cm^2)
Uncoated bar	7520	17561	9363
FGM coated bar	21521	49518	35512

Table 9 EIS results for samples immersed for 56 days at 298 K.

Specimen		R_s (Ω.cm^2)	$R_s + R_{ct}$ (Ω.cm^2)	Z_w (Ω.cm^2)
Uncoated bar		255.95	975.5	1106
FGM coated bar		16990	50227	4.306 10^{12}

3.4. Theoretical simulation

This section includes studying the coating layers of applied three metals (Cu/Zn/Sn system) as (FGC) under varying thermal conditions and in an ionic environment containing Na^+ and Cl^- ions, using molecular dynamics simulations. These ions are standard components in many environmental and industrial systems, playing a significant role in modifying adsorption behavior and surface stability. By analyzing variations in temperature, potential energy, and kinetic energy over simulation timescales extending to 3000 picoseconds, the study evaluates the system's ability to adapt the thermal stress and ionic interactions. Density functional theory (DFT) is a quantum mechanical modeling method used to investigate the electronic structure of materials based on their electron density rather than many-body wavefunctions. In this study, DFT is employed to design and optimize the bulk crystal structures of copper (Cu), zinc (Zn), and tin (Sn) using the generalized gradient approximation (GGA) with the Perdew-Burke-Ernzerhof (PBE) functional [52-54]. After bulk optimization, surface cleavage is performed by investigating slab models along the low-energy (001) crystallographic planes for three metals (Cu, Zn, and Sn) each separated by a 15 Å vacuum layer to eliminate periodic image interactions. These individual surfaces are then assembled into a layered heterostructure to simulate interfacial interactions [55, 56]. To evaluate thermal stability and dynamic behavior, Forcite molecular dynamics simulations are carried out under the NVT ensemble using a Nosé–Hoover thermostat at various time scales (1000, 2000, and 3000 ps), with temperature variations monitored throughout. Finally, sorption isotherm calculations are conducted at three distinct temperatures (298, 308, and 318 K) to assess the adsorption behavior of (Cl^-) ions through the engineered surface [57]. The results revealed the temperature-dependent sorption capacity and surface reactivity, supporting the material's potential for applications in surface catalysis and interfacial material design [58, 59]. Surface cleavage is important for controlling the contact area between the material and adsorbate ions, thereby enhancing interaction behavior. Figure 16 illustrates the geometrically optimized crystal units of Cu, Zn, and Sn individually, followed by surface cleavage along the (001) plane for each. A slab model incorporating all three elements (three-layer: Cu–Zn–Sn-based structure) is constructed. Figure 16a shows face-centered cubic (FCC) for Cu, where cleavage along the (001) plane produces a layered surface with minimal atomic distortion after relaxation, reflecting metallic bonding and high structural symmetry. Figure 16b presents a hexagonal close-packed for Zn crystal, where the (001) plane corresponds to the basal plane; post-optimization, the structure exhibits well-preserved atomic stacking

due to anisotropic bonding. In Figure 16c, tetragonal β-Sn displays a more complex bonding environment; cleavage and relaxation along the (001) plane expose hexagonal tunnel-like features, indicating directional bonding and structural anisotropy. Finally, Figure 16d shows the integrated Cu–Zn–Sn slab model, revealing a vertically aligned, chemically ordered structure after optimization. This configuration is essential for simulating surface properties, interface formation, and heterojunction behavior in multicomponent systems. The geometry optimizations performed for each system minimize surface energy and ensure structural realism, making the resulting slab models suitable for further electronic structure and surface interaction studies [60, 61].

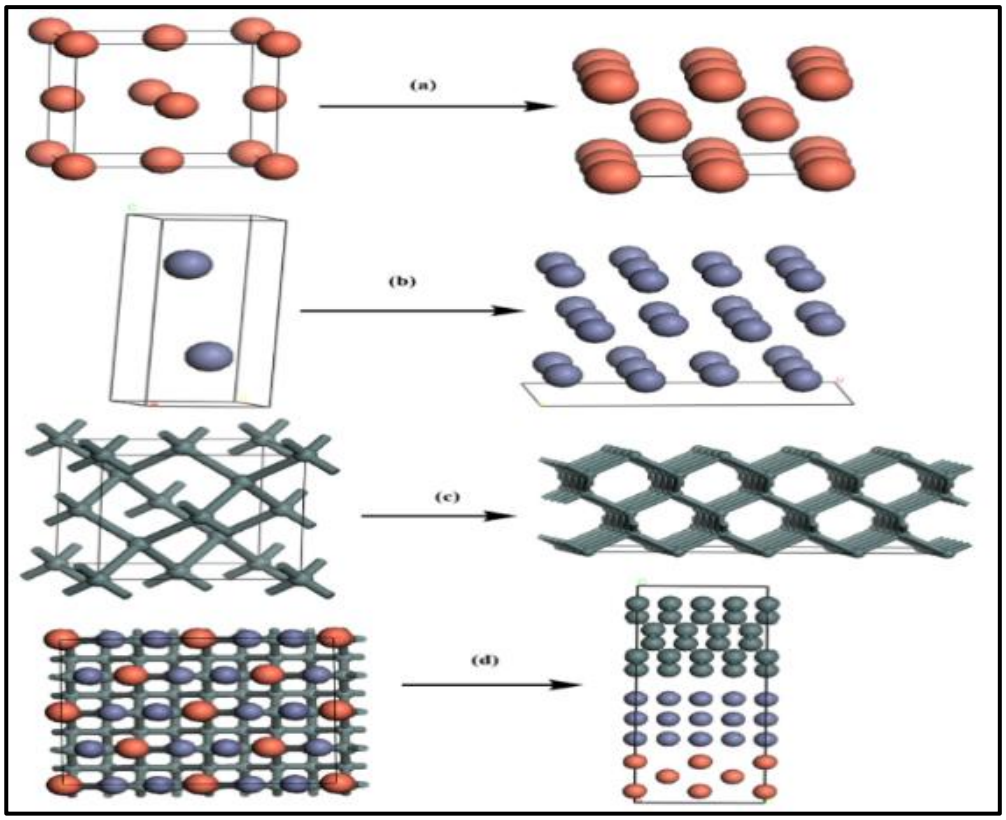

Figure 16 Geometrically optimized crystal structures with (001) surface cleavage for: (a) Cu, (b) Zn, (c) Sn, and (d) a three-layer Cu–Zn–Sn slab model.

The Cu-Zn-Sn layered structure exhibits significant variations in potential and kinetic energy over time (see Figures 17 and 18). This interplay between potential and kinetic energy highlights the material's adaptability to dynamic conditions, influencing its thermal conductivity and phase transition behavior. These insights are essential for optimizing such composites in electronic and structural applications, as they inform predictions of energy storage, dissipation, and equilibrium behavior. Figure 17 shows the variation in potential energy (E_{pot}) over three simulation intervals (1000, 2000, and 3000 ps) in the absence of NaCl as medium. Panel (a) shows a rapid initial decline in E_{pot}, stabilizing around ~2090 kcal/mol, indicative of system relaxation. Panel (b) reveals fluctuations within a narrow range (~2075–2110 kcal/mol), suggesting a dynamically stable state. Panel (c) confirms this behavior over a longer timescale, with E_{pot} maintaining a consistent average despite natural thermal fluctuations,

demonstrating structural equilibrium in the absence of external ionic media [62]. Figure 18 shows the kinetic energy (E_{kin}) over the same simulation intervals. Across all panels, E_{kin} fluctuates around a relatively stable average (approximately 60–75 kcal/mol), confirming that the system rapidly achieves and maintains thermal equilibrium. These fluctuations, characteristic of thermal motion at constant temperature, show no drift or trend, further validating the stability of the kinetic energy profile during the simulation [63].

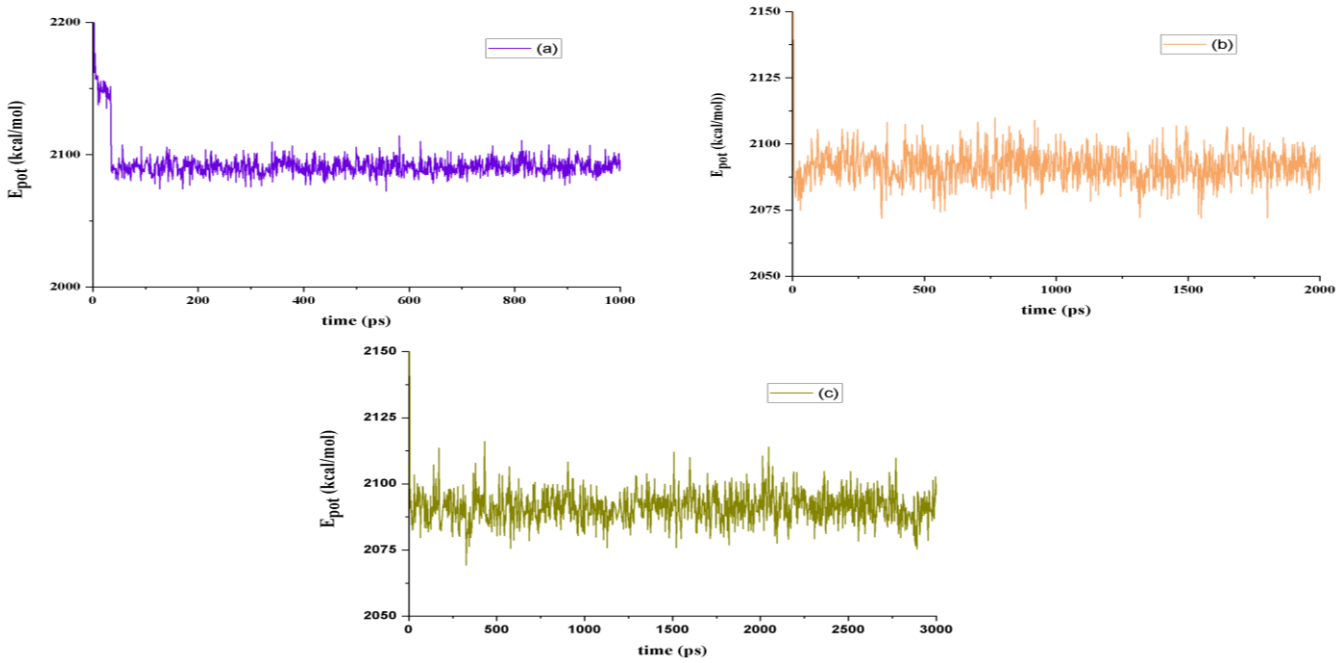

Figure 17 Correlation of potential energy with simulation time for the Cu/Zn/Sn layered system at: (a) 1000 ps, (b) 2000 ps, and (c) 3000 ps, in the absence of NaCl medium.

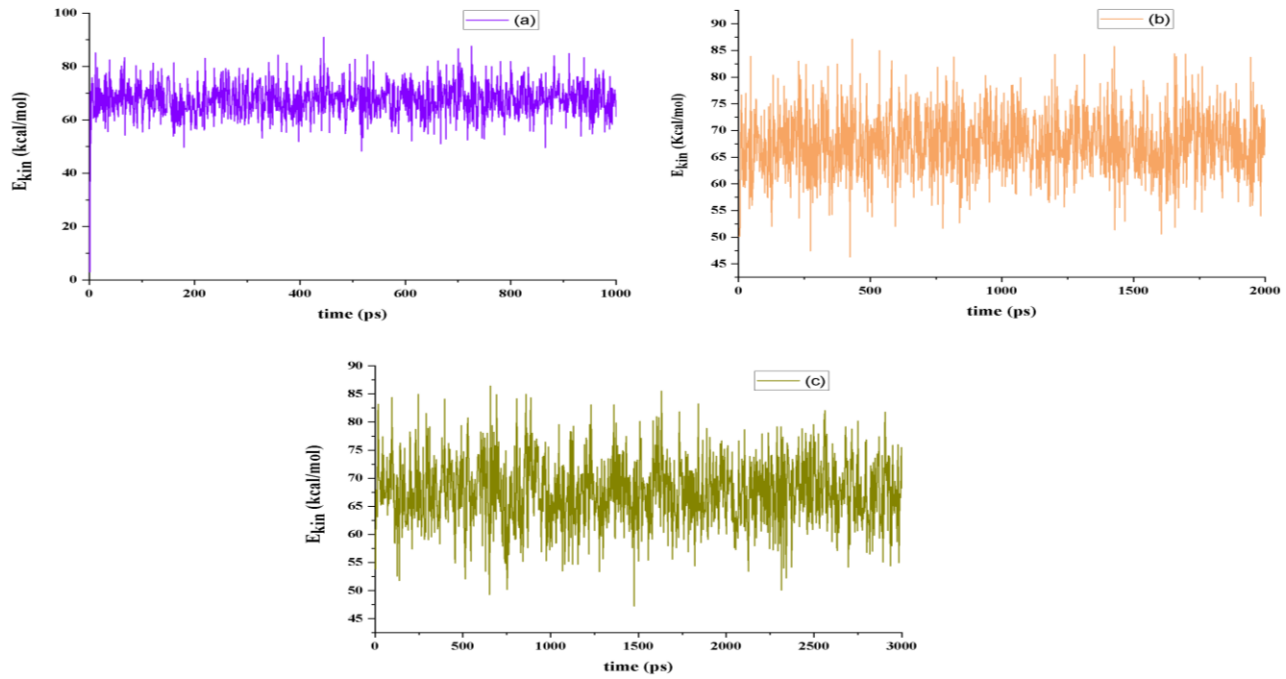

Figure 18 Correlation of kinetic energy with time for the Cu-Zn-Sn layered system at: (a) 1000 ps, (b) 2000 ps, and (c) 3000 ps without NaCl solution.

Figures 19 and 20 illustrate the potential and kinetic energy variations in the FGC under the influence of Na^+ and Cl^- during molecular dynamics simulations. The potential energy (E_{pot}) graph provides insights into atomic interactions, structural stability, and energy redistribution, while the kinetic energy (E_{kin}) captures atomic motion and thermal effects, including the movement of Na^+/Cl^- ions through the layers. Figure 19 shows the evolution of E_{pot} over 1000, 2000, and 3000 ps in the presence of (NaCl) as medium. In all cases, the system exhibits fluctuations around ~2100 kcal/mol. Compared to the NaCl-free case, these fluctuations are slightly broader, suggesting increased dynamic response due to Cl^- ion interactions. A sharp energy drops at ~250 ps (see Figure 19b) reflects structural rearrangement as ions integrate into the lattice, followed by stabilization. These variations suggest atomic rearrangement, phase transitions, or localized bonding changes, providing insight into the system's thermal resilience and structural adaptation [64]. Figure 20 shows the corresponding E_{kin} profiles over the same time intervals. In all panels, kinetic energy fluctuates around a stable average (~85–95 kcal/mol), consistent with normal thermal motion at constant temperature and indicative of thermal equilibrium. Initial fluctuations in kinetic energy indicate rapid atomic adjustments driven by Na^+/Cl^- interactions, leading to increased vibrational activity. Over shorter timescales (up to 1000 ps), energy oscillates between 70 and 95 kcal/mol, while over longer periods (2000-3000 ps), it ranges from 65 to 105 kcal/mol, reflecting progressive interactions. Together, these analyses highlight the energetic interplay in the triple-layered system, showing how sodium chloride ions affect energy distribution, stability, and atomic movement [65].

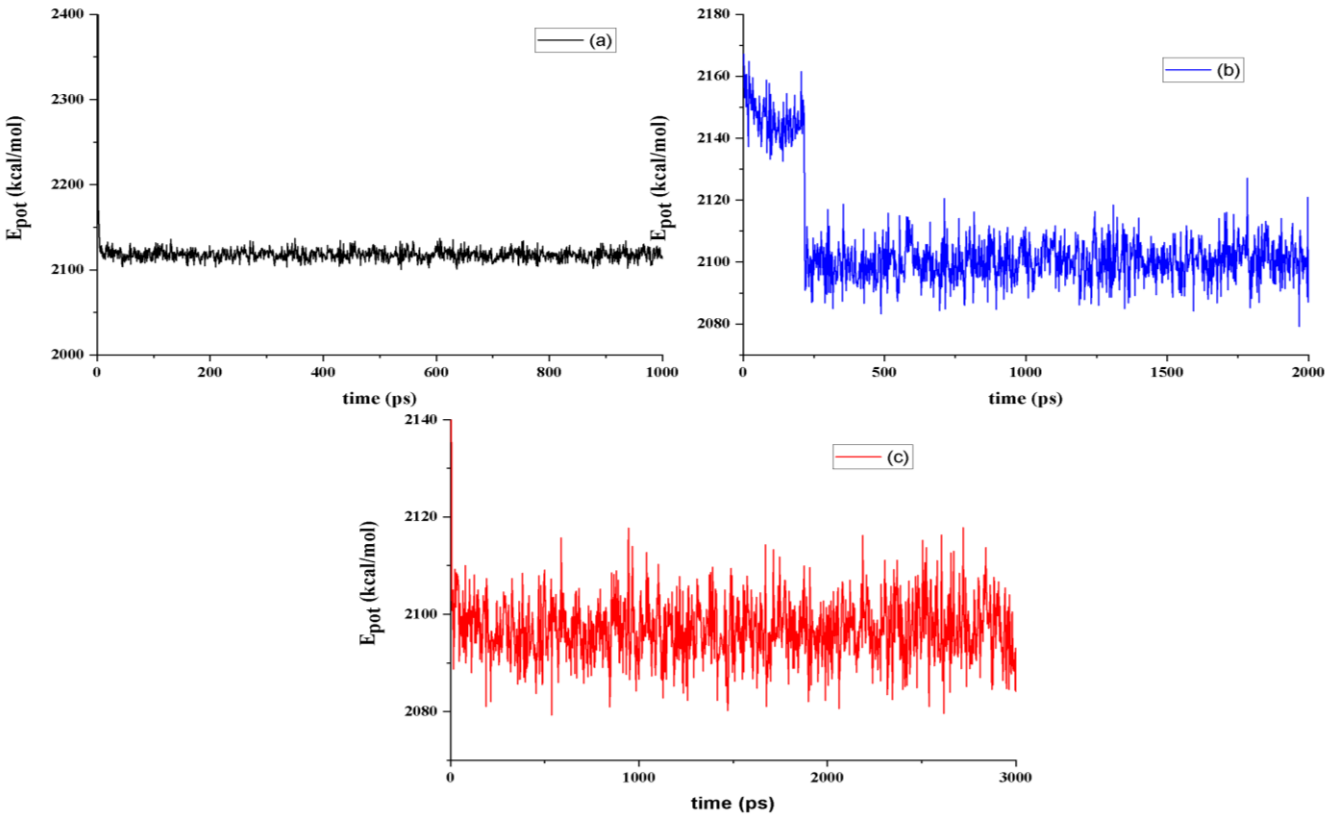

Figure 19 Potential energy variation over time for FGC at: (a) 1000 ps, (b) 2000 ps, and (c) 3000 ps, in the presence of NaCl medium.

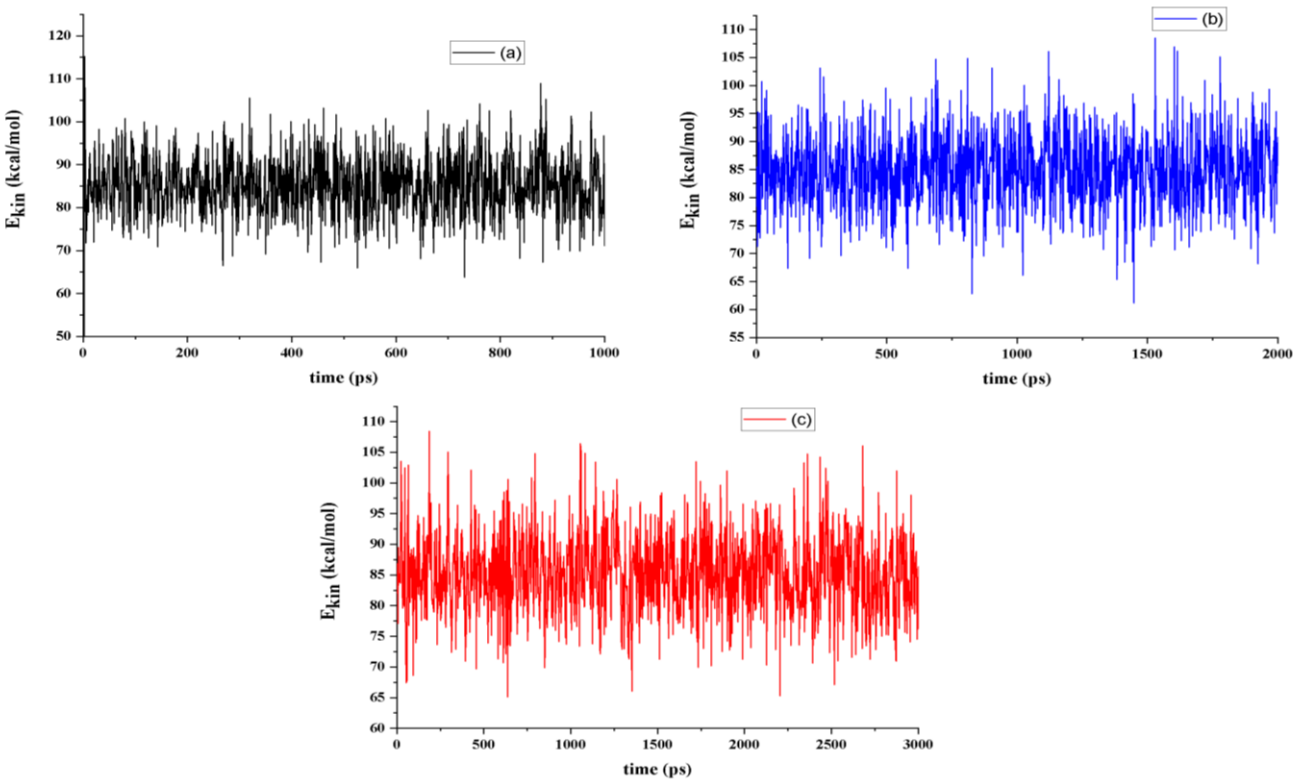

Figure 20 Time- dependent kinetic energy profile with time in the dynamic simulation process for Cu/Zn/Sn layered system at: (a) 1000 ps, (b) 2000 ps, and (c) 3000 ps, in the presence of NaCl solution.

In the dynamic simulation of a Cu/Zn/Sn layered system (FGC) over 1000 ps, as presented in Figure 21, the migration of Na^+ and Cl^- ions significantly influence the structural and electronic properties. Initially, the ions remain relatively confined, but as the simulation progresses, thermal agitation and electrostatic interactions drive their diffusion into different layers. By the final stage, the ions are widely dispersed, modifying interlayer distances and affecting charge distribution. This migration impacts the stability, conductivity, and application potential of the system [66].

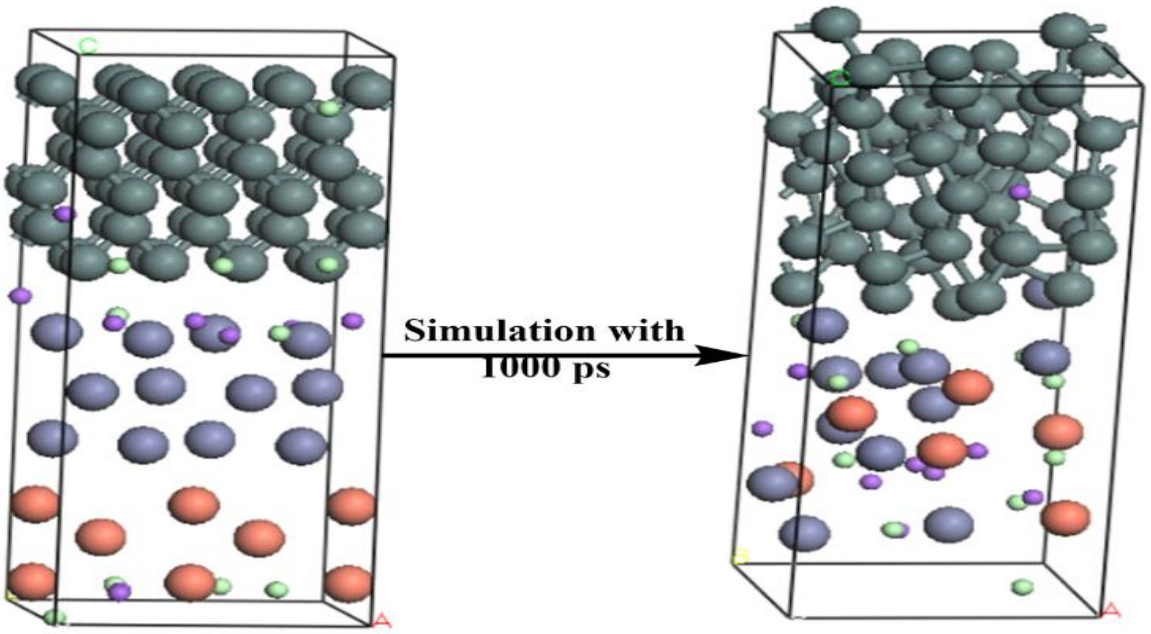

Figure 21 Structural evolution of the layered system: (a) before and (b) after 1000 ps dynamic simulation (Na: Purple, Cl: Green).

Over 2000 ps (see Figure 22), the migration of Na^+ and Cl^- ions continue to evolve, influencing the system's properties and structure. Compared to the 1000 ps simulation, prolonged exposure increases diffusion, resulting in further redistribution and deeper incorporation into the metallic framework. This increases interlayer distances, conductivity, and phase formation. Persistent interactions of Na^+ and Cl^- with Cu, Zn, and Sn atoms may induce localized defects or structural reconfigurations, which are crucial for tuning the system's behavior [67].

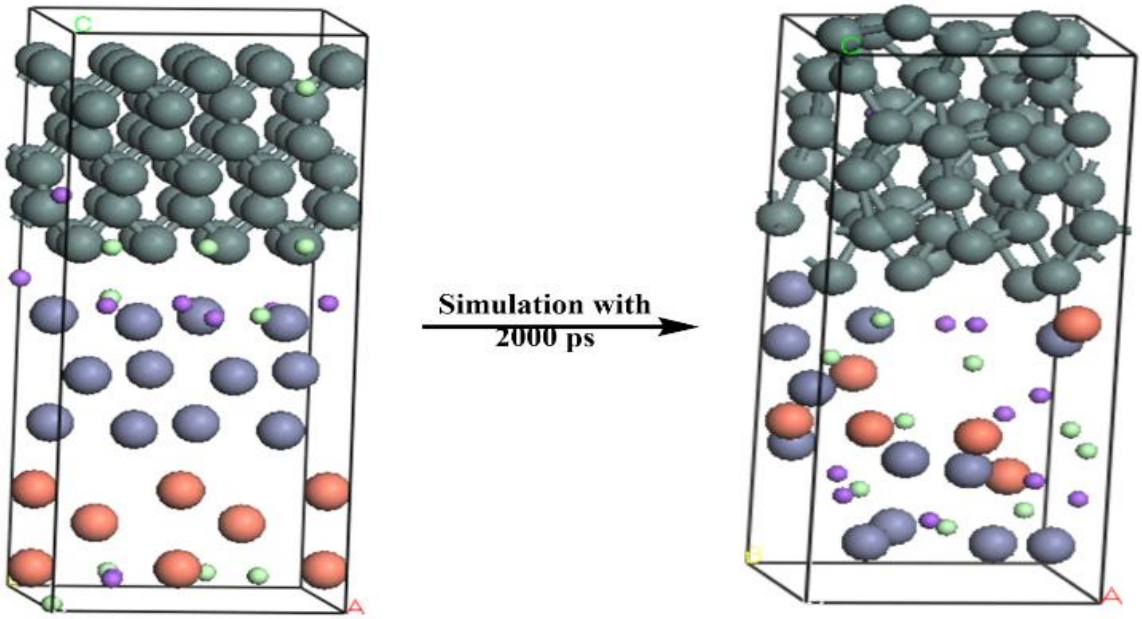

Figure 22 Atomic rearrangement in the layered system: (a) before, and (b) after 2000 ps dynamic simulation (Na= purple, and Cl= green).

Over 3000 ps (Figure 23), the migration of Na^+/Cl^- ions become more pronounced, accompanied by significant structural deformation and deeper integration into the metallic-framework. This extended period of time promotes increased ionic diffusion, resulting in notable changes in interlayer spacing and charge distribution. Na^+/Cl^- interactions with the Cu, Zn, and Sn layers lead to rapid atomic adjustments, increased dispersion, and kinetic mixing, where Cu atoms diffuse through the Zn layer toward Sn layer, inducing phase transitions. The continuous movement of Na^+ and Cl^- affects the system's stability and conductivity, potentially forming new phases or defects within the layers [68].

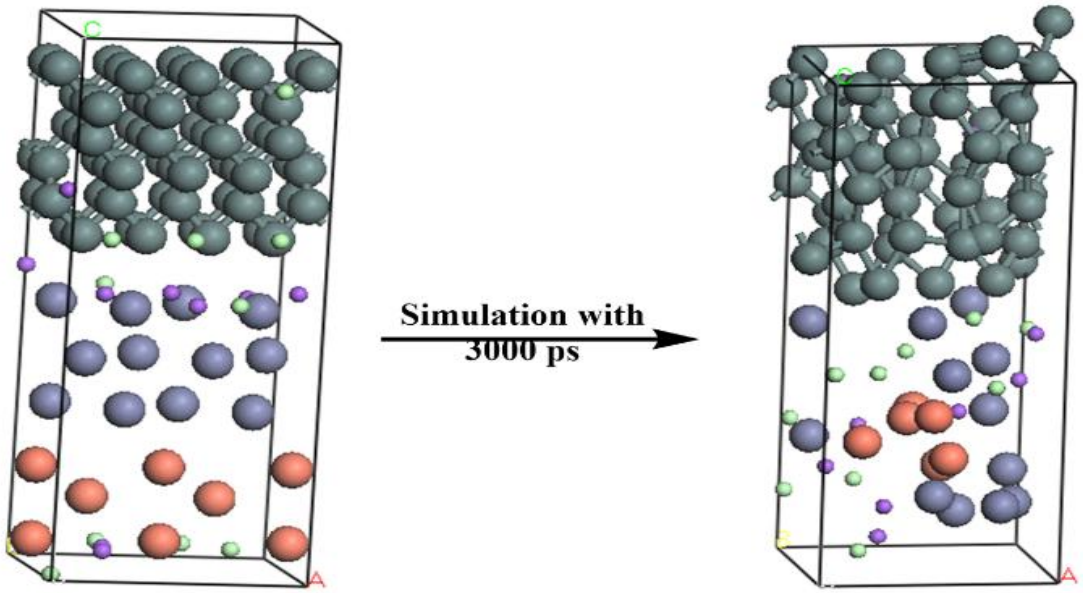

Figure 23 Structural transformation of the multi-layered system: (a) pre-simulation and (b) post-simulation configurations following 3000 ps dynamic analysis (Na: purple, Cl: green).

Typically, sorption decreases with increasing temperature in exothermic systems, as elevated thermal energy disrupts interactions between the sorbate and the sorbent. In contrast, endothermic processes, often involving structural changes or bulk diffusion, can exhibit increased sorption capacity at higher temperatures due to enhanced molecular mobility and the ability to overcome energy barriers. The energy distribution function, P(E), represents the probability of finding sorption sites with a particular energy (E). Surfaces, especially heterogeneous ones, contain sites with different energies due to structural or chemical variations. P(E) is useful in understanding the heterogeneity of the adsorbent [69, 70]. Figure 24 shows the energy distribution function versus the sorption energy of Na^+ and Cl^- atoms at (298, 308, and 318 K). Na shows a narrow distribution, indicating a uniform adsorption surface, while Cl shows broader, multi-peaked curves, especially at 318 K, suggesting heterogeneous sites, likely within interlayers. At 298 K, adsorption is dominated by physisorption, where weak Van der Waals forces lead to low energy levels and minimal structural change. As temperature rises to 308 K, thermal agitation increases molecular mobility, promoting stronger adsorbate–sorbent interactions and increasing the number of adsorption sites and energy states. At 318 K, sorption shifts toward chemisorption, which potentially alters the surface structure, increasing energy distribution heterogeneity. This progression highlights the effect of temperature on sorption efficiency, mechanism, and material stability [71,72].

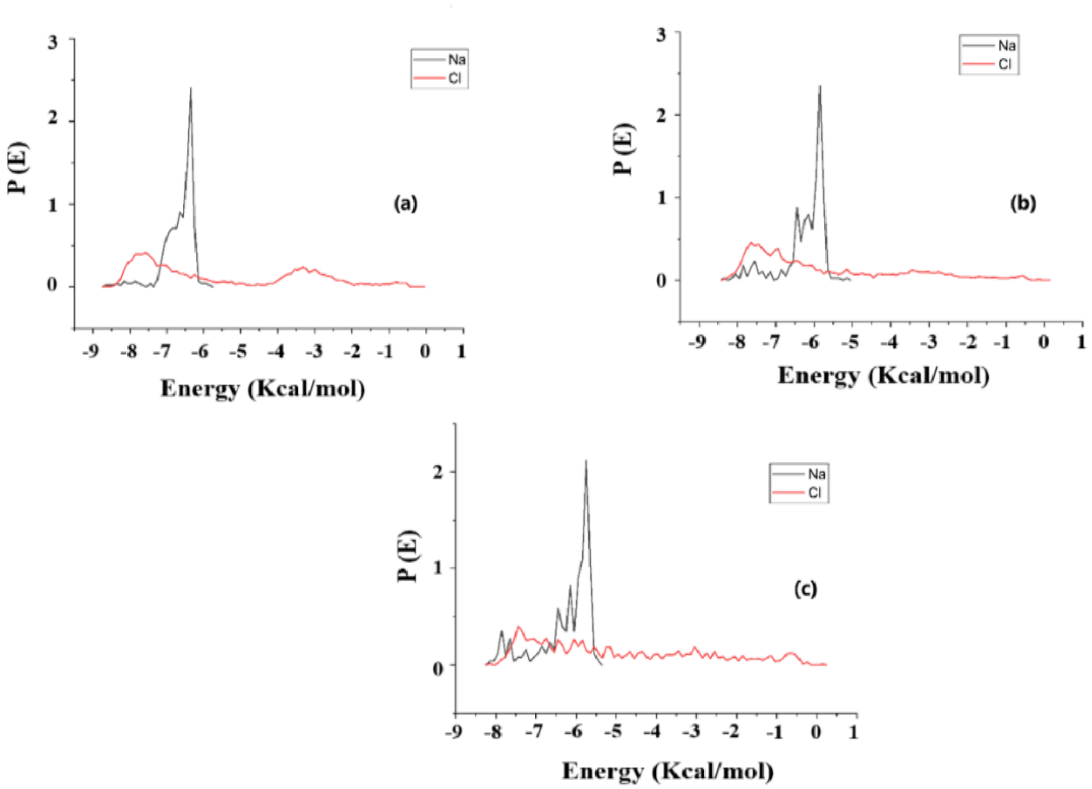

Figure 24 Energy distribution of Na^+ and Cl^- ions during the sorption process at: (a) 298 K, (b) 308 K, and (c) 318 K.

The average loading of Na^+ and Cl^- ions on the Cu-Zn-Sn layered system (FGC) surface is strongly influenced by temperature, as outlined in Figure 25 using sorption isotherm analysis. At 298 K, adsorption is primarily governed by weak Van der Waals forces, leading to moderate ion attachment without significant penetration into the bulk structure. At 308 K, increased thermal energy promotes ion mobility, allowing for stronger surface interactions and multilayer adsorption, which alters charge distribution and surface energy. At 318 K, chemisorption dominates, increasing the average loading of ions and rising the material's adsorption capacity. These temperature-dependent behaviors highlight the dynamic nature of ion sorption, demonstrating how increasing thermal agitation facilitates deeper ion incorporation. Figure 26 confirms the ionic distribution expressed in the field map at various temperature [73,74].

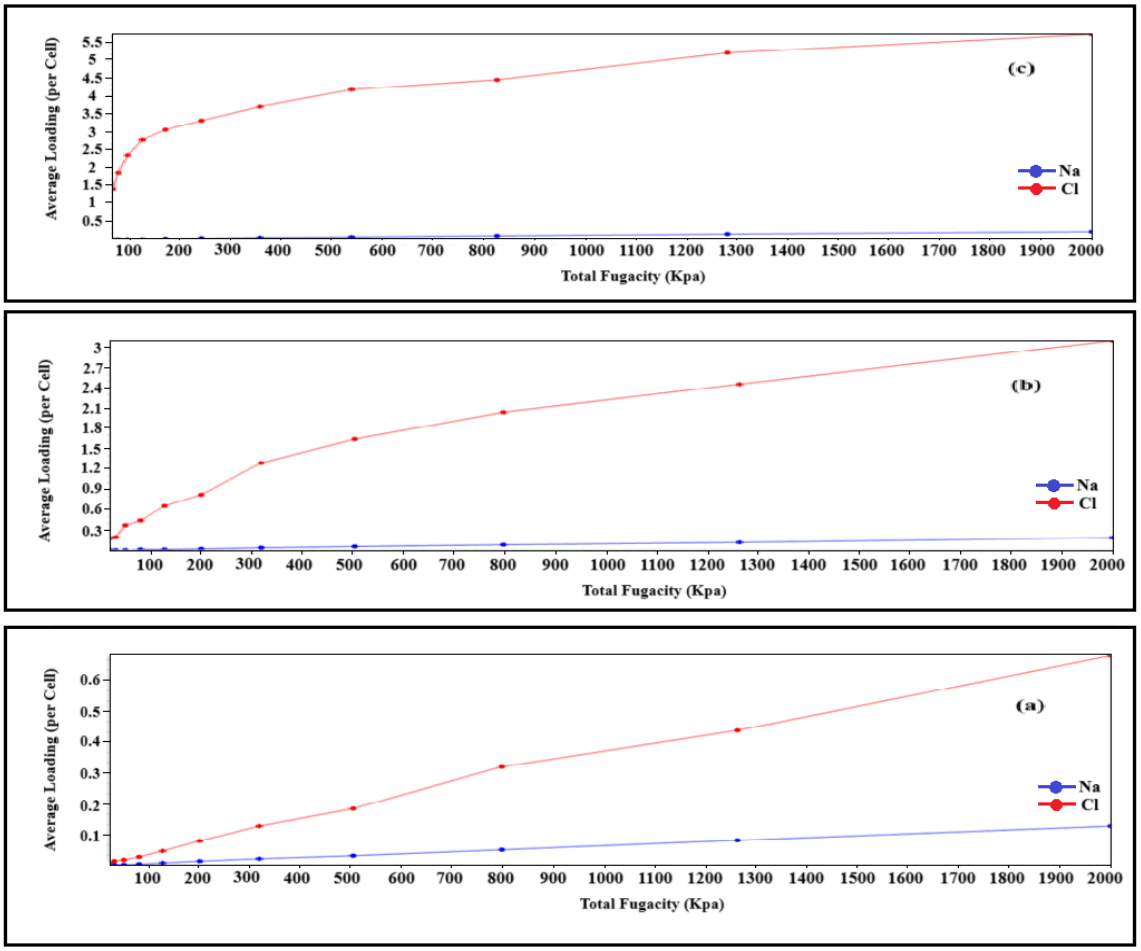

Figure 25 Sorption isotherm and average loading of Na^+/Cl^- ions on the surface of FGC at: (a) 298 K, (b) 308 K, and (c) 318 K.

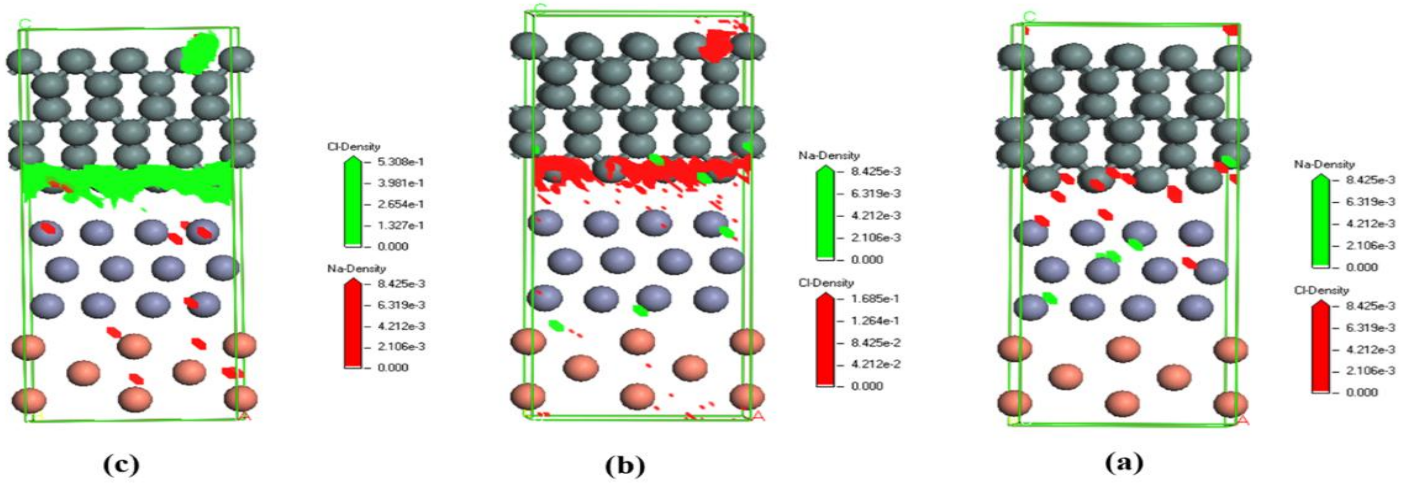

Figure 26 System-field color maps of (Na^+/Cl^-) ions sorption with average loading at different temperatures: (a) 298 K, (b) 308 K, and (c) 318 K.

4. CONCLUSIONS

The application of Cu/Zn/Sn nanoparticles as functionally graded coatings (FGCs) via a modified spray technique significantly enhanced both the corrosion resistance and mechanical integrity of steel rebars exposed to chloride-rich environments. Electrochemical analysis showed that at 298 K, after 28-days of immersion in (3.5 wt.%) sodium chloride solution, the coated specimens achieved the lowest corrosion current density of 0.299×10^{-7} A/cm², accompanied by a peak inhibition efficiency of 97.92%. Electrochemical impedance spectroscopy further confirmed the coating's superior barrier properties, with the maximum solution resistance recorded at 21,521 Ω·cm² and the minimum porosity level at 2.15×10^{-20}% at 308 K under the same exposure duration. In terms of mechanical performance, the coated steel exhibited a surface hardness of 221.4 HV compared to 195.8 HV for the uncoated counterpart, indicating improved wear resistance. These results demonstrate the coating's ability to deliver long-term protection in harsh marine conditions. Moreover, theoretical simulations confirmed that the Cu/Zn/Sn layered structure maintained its stability and adapted effectively to ionic and thermal environments, thereby reinforcing the reliability of the experimental results.

References

[1] B. Joseph, G. NarendraKumar, G. Mageshwaran, J. Jeevahan, V.Sriram, R. Raj, Int. J. Ambient Energy 40 (2018) 9. DOI: 10.1080/01430750.2018.1437564
[2] E. T. Abdullah, M. R. Khasheet, Z. N. Hasheem, Experimental and Theoretical NANOTECHNOLOGY 9 (2025) 373. https://doi.org/10.56053/9.S.373
[3] S. R. Yeomans, HKIE Transactions 2 (1995) 17. https://doi.org/10.1080/1023697X.1995.10667682
[4] O. Alabdali, A. Guessab, Filomat, 34 (2020) 601. https://doi.org/10.2298/FIL2002601A.
[5] M. Sulaiman, E. M. Hadi, Experimental and Theoretical NANOTECHNOLOGY 9 (2025) 431. https://doi.org/10.56053/9.S.431
[6] R. Anaee, M. Abbas, S. Abdul Maged, S. Naser, S. Hamdi, H. Yousif, N. AL-Bahnam, T. Anai, I, Experimental and Theoretical NANOTECHNOLOGY 9 (2025) 449. https://doi.org/10.56053/9.S.449
[7] F. Moreno, M.A. Jakab, N. Tailleart, M. Goldman, J.R. Scully, Mater. Today 11 (2008) 14. https://doi.org/10.1016/S1369-7021(08)70203-7
[8] M. V. Orlov, W. O. Badeghaish, J. Physics: Conference Series 1990 (2021) 012001. https://doi.org/10.1088/1742-6596/1990/1/012001
[9] H. Wang, S. Hsieh, B. Peng, X. Zhou, Infrared Phys. & Technol. 77 (2016) 316. https://doi.org/10.1016/j.infrared.2016.06.015
[10] G. E. Alkinani, A. R. J. Katae, M. RASHEED, Experimental and Theoretical NANOTECHNOLOGY, 10 (2026) 1027. https://doi.org/10.56053/10.S.1027
[11] P. Ranjan, R. Kumar, R. S. Walia, Rev. J. Physics: Conference Series 2007 (2021) 012068. https://doi.org/10.1088/1742-6596/2007/1/012068
[12] J. Jeon, H. Fang, Z. Lai, Z. Yin, Key Eng. Mater. 280-283 (2005) 1851. 10.4028/www.scientific.net/KEM.280-283.1851
[13] F. Boudou, A. E. Sabar, M. I. Majeed, A. M. Ibraham, R. Jamal, A. Rashid, A. Belakredar, M. Bendahmane-Salmi, M. RASHEED, R. RASHEED, T. Saidani, H. D. Al-Bahadli, Experimental and Theoretical NANOTECHNOLOGY, 10 (2026) 821. https://doi.org/10.56053/10.S.821

[14] J. Chen, S. Tu, J. Chinese Institute Eng. 27 (2004) 805. https://doi.org/10.1080/02533839.2004.9670931
[15] A. R. J. Katae, H. H. Hussein, A. S. Jaber, M. A. Sarhan, M. RASHEED, Experimental and Theoretical NANOTECHNOLOGY, 10 (2026) 725. https://doi.org/10.56053/10.2.725
[16] W. Y. Lee, D.P. Stinton, C. Berndt, F. Erdogan, Y. Lee, Z. Mutasim, J. Am. Ceram. Soc. 79 (1996) 3003. https://doi.org/10.1111/j.1151-2916.1996.tb08070.x
[17] M. Enneffati, M. Rasheed, B. Louati, K. Guidara, R. Barillé, Optical and Quantum Electronics, 51 (2019) 1. https://doi.org/10.1007/s11082-019-2015-53
[18] M. H. Allahyarzadeh, M. Aliofkhazraei, A. R. Sabour Rouhaghdam, V. Torabinejad, Canadian Metall. Q. 55 (2016) 303-311. 10.1080/00084433.2016.1190542
[19] J. Singh, S. S. Chatha, H. Singh, J. Therm. Spray Technol. 27 (2018) 1371. https://doi.org/10.1007/s11666-018-0802-3
[20] A. U. Ammar, M. Shahid, M. K. Ahmed, M. Khan, A. Khalid, Z. A. Khan, Mater. 11 (2018) 332. doi:10.3390/ma11030332
[21] S. Banthia, S. Sengupta, S. Das, K. Das, Surf. Coat. Technol. 374 (2019) 833. https://doi.org/10.1016/j.surfcoat.2019.06.050
[22] N. A. Ismail, R. A. Shakoor, N. Al-Qahtani, R. Kahraman, ACS Omega 8 (2023) 30838. https://doi.org/10.1021/acsomega.2c06406
[23] P. Ranjan, R. Kumar, R. S. Walia, V. K. Yadav, Phys. Scr. 99 (2024) 085045. 10.1088/1402-4896/ad6494
[24] M. Sathish, N. Radhika, B. Saleh, Sci. Rep. 14 (2024) 22272. https://doi.org/10.1038/s41598-024-72208-2
[25] R. Marquardt, M. Biegler, M. Rethmeier, Prog. Addit. Manuf. (2024) 6. https://doi.org/10.1007/s40964-024-00879-4
[26] H. M. I. Al-Zuhairi, I. Alshalal, H. H. Abbood, M. Al Nuaimi, Experimental and Theoretical NANOTECHNOLOGY, 10 (2026) 1093. https://doi.org/10.56053/10.S.1093
[27] W. M. Abd El-Gawad, E. A. Mossalam, M. Gharieb, Innov. Infrastruct. Solut. 9 (2023) 16. https://doi.org/10.1007/s41062-023-01279-3
[28] L.Yan, W. Deng, N. Wang, X. Xue, J. Hua, Z. Chen, A Rev. polymers 14 (2022) 4782. https://doi.org/10.3390/polym14214782
[29] H. M. I. Al-Zuhairi, I. Alshalal, H. H. Abbood, M. Al Nuaimi, Experimental and Theoretical NANOTECHNOLOGY, 10 (2026) 855. https://doi.org/10.56053/10.S.855
[30] A. J. Hussein, M. N. Al-Darraji, M. Rasheed, M. A. Sarhan, IOP Conference Series: Earth and Environmental Science, 1262 (2023) 022005. https://doi.org/10.1088/1755-1315/1262/2/022005.
[31] M. Enneffati, B. Louati, K. Guidara, M. Rasheed, R. Barillé, Journal of Materials Science: Materials in Electronics, 29 (2018) 171. https://doi.org/10.1007/s10854-017-7901-7.
[32] M. Rasheed, O. Y. Mohammed, S. Shihab, A. Al-Adili, Journal of Physics: Conference Series, 1795 (2021) 012042. https://doi.org/10.1088/1742-6596/1795/1/012042.
[33] M. Rasheed, et al., Journal of Advanced Biotechnology and Experimental Therapeutics, 6 (2023) 495. https://doi.org/10.5455/jabet.2023.d144.
[34] E. Kadri, et al., Journal of Alloys and Compounds, 705 (2017) 708. https://doi.org/10.1016/j.jallcom.2017.02.117.
[35] A. Jaber, M. Ismael, T. Rashid, M. A. Sarhan, M. Rasheed, I. M. Sala, Eureka: Physics and Engineering, 4 (2023) 29. https://doi.org/10.21303/2461-4262.2023.002770.
[36] H. A. Abdulaah, A. M. Al-Ghaban1, R. Anaee, A. Khadom, M. Kadhim, J. Electrochem. Sci. Eng 13 (2023) 115.

[37] S. Naser, R. A. Anaee, H. A. Jaber, Adv. Mater. Process. Technol. (2024) 12. https://doi.org/10.1080/2374068X.2024.2306568
[38] A. Sharma, H. Seo, B. Ahn, Coatings 10 (2020) 117. https://doi.org/10.3390/coatings10020117
[39] K. Gu, R. Hao, J. Guo, A. Aierken, X. Liu, F. Chang, Y. Li, G. Wei, B. Liu, L. Wang, S. Sun, X. Ma , J. Electronic Mater. 49 (2020) 18191826. https://doi.org/10.1007/s11664-019-07890-4
[40] M. Karthik, J. Abhinav, K. V. Shankar, Met. Mater. Int. 27 (2021) 1915. https://doi.org/10.1007/s12540-020-00899-z
[41] S.D. Kumar, R. Kumar, Int. J. Res. Appl. Sci. Eng. Technol.7 (2019) 911. https://doi.org/10.22214/ijraset.2019.11154
[42] D. Kherifi, A. Keziz, M. Rasheed, A. Oueslati, Ceramics International, 50 (2024) 1. https://doi.org/10.1016/j.ceramint.2024.05.317.
[43] P. Refait, A. Grolleau, M. Jeannin, C. Rémazeilles, R. Sabot, Corros. Mater. Degrad. 1 (2020) 198. https://doi.org/10.3390/cmd1010010
[44] A. Goyal, H. S. Pouya, E. Ganjian, P. Claisse, Arab. J. Sci. Eng. 43 (2018) 5035. https://doi.org/10.1007/s13369-018-3303-2
[45] J. Alcántara, D. Fuente, B. Chico, J. Simancas, I. Díaz, M. Morcillo, Mater. 10 (2017) 406. https://doi.org/10.3390/ma10040406
[46] S. A. Naser, R. Anaee, H. A. Jaber, Adv. Mater. Process. Technol. 1 (2024) 12. https://doi.org/10.1080/2374068X.2024.2306568
[47] M. Gagné, F. E. Goodwin, M. Leeuwen, Conference: 9th Int. Symp. Steel Bridges 1 (2018) 7. https://www.researchgate.net/publication/342751453
[48] A. Al-Ghaban, H. Abdullah, R. Anaee, S. Naser, A. Khadom, J. Eng. Res. 12 (2023) 299. https://doi.org/10.1016/j.jer.2023.11.020
[49] A. Zubaidi, L. M. Asaad, I. Alshalal, M. Rasheed, Journal of the Mechanical Behavior of Materials, 32 (2023) 1. https://doi.org/10.1515/jmbm-2022-0302.
[50] Z. Liang, K. Jiang, T. Zhang, Z. Dou, Mater. Corros. 71, (2019) 11. https://doi.org/10.1002/maco.201911338
[51] J. Creus, H. Mazille, H. Idrissi, Surf. Coat. Technol. 130, (2000) 224. https://doi.org/10.1016/S0257-8972(99)00659-3
[52] P. Singh, M. K. Harbola, Oxf. Open Mater. Sci. 1 (2021) 22. https://doi.org/10.1093/oxfmat/itab018.
[53] A. Issa, H. Ibraheem, D. S. El-Sayed, J. J. Mol. Model. 30 (2024) 19. https://doi.org/10.1007/s00894-023-05815-x
[54] A. Alkhafaji, H. M. Ahmed, B. K. Queen, A. Issa, G. M. Sulaiman, A. ELkashef, D. El-Sayed, J. Organomet. Chem.1022 (2024) 123417. https://doi.org/10.1016/j.jorganchem.2024.123417.
[55] H. Peng, J. P. Perdew, Phys. Rev. B95 (2017) 081105. https://doi.org/10.1103/PhysRevB.95.081105
[56] G. K. H. Madsen, Phys. Rev. B75 (2007), 195108. https://doi.org/10.1103/physrevb.75.195108.
[57] D. S. El-Sayed, J. Mol. Model. 29 (2023) 1-16. https://doi.org/10.1007/s00894-023-05501-y
[58] S. Shimizu, N. Matubayasi, Langmuir 37 (2021) 11008. https://doi.org/10.1021/acs.langmuir.1c01576.
[59] J. Wang, X. Guo, Chemosphere 258 (2020) 127279. https://doi.org/10.1016/j.chemosphere.2020.127279.
[60] S. Su, A. Sun, G. Li, Y. Ding, M. Xu, Case Stud. Therm. Eng.61 (2024) 105145. https://doi.org/10.1016/j.csite.2024.105145.
[61] J. Magliaro, W. Altenhof, A. T. Alpas, Thin-Walled Struct. 180 (2022) 109808. https://doi.org/10.1016/j.tws.2022.109808.

[62] H. Ibraheem, Y. Al-Majedy, A. Abdullah Issa, E. Yousif, Trends Sci. 21 (2024) 7374. https://doi.org/10.48048/tis.2024.7374.
[63] A. Waleed, D. Younus, A. A. Issa, H. R. Obayes, M. S. Ali, D. S. El-Sayed, Russ. J. Gen. Chem. 94 (2024) 2676-2688. https://doi.org/10.1134/S107036322410013X
[64] H. Ibraheem, A. S. Shubrem, Y. K. Al-Majedy, A. Abdullah Issa, AIP Conf. Proc. 2443 (2022) 030044. https://doi.org/10.1063/5.0091889.
[65] Y.K. Al-Majedy, H.H. Ibraheem, A.A. Issa, A. Alamiery, Int. J. Corros. Scale Inhib. 12 (2023) 1028. https:// doi. org/ 10. 17675/ 2305- 6894- 2023- 12-3- 14.
[66] A. A. Issa, A. Alkhafaji, F. S. Abdulwahid, R. A. Al-Obaidy, M. D. Kamel, A. J. Haider, A. Al-Shaham, J. Inorg. Organomet. Polym. Mater. 34 (2024) 4713. https://doi.org/10.1007/s10904-024-03116-1.
[67] A. Abdullah Issa, M. D. Kamel, D. S. El-Sayed , J. Mol. Model. 30 (2024) 106. https://doi.org/10.1007/s00894-024-05896-2.
[68] A. A. Issa, H. R. Obayes, J. Mol. Model. 26 (2020) 292. https://doi.org/10.1007/s00894-020-04558-3.
[69] Y. K. Al-Majedy, H. Ibraheem, A. Abdullah Issa, , AIP Conf. Proc. 2593 (2023) 060002. https://doi.org/10.1063/5.0113038.
[70] Gegentana, L. Cui, L. Zhou, X. Du, J. Phys. Chem. B, 128 (2024) 8484. 10.1021/acs.jpcb.4c02413
[71] M. Nguyen, V. Glezakou, J. Lonergan, B. McNamara, P. D. Paviet, R. Rousseau, J. Mol. Liq. 326 (2021) 115262. 10.1016/j.molliq.2020.115262
[72] Abeer F. Al-Attar, Hussein A. Jaber and Rana A. Anaee, Produce solid oxide fuel cell anodes as $(BaTiO_3)_{100-x}$–$(MgO)_x$ for clean energy, Results in Engineering. 2023; 19: 101327. https://doi.org/10.1016/j.rineng.2023.101327
[73] J. Xu, F. Tian, F. Zhu, Z. Pang, Z. Ma, H. Miao, X. Zhang, C. Han, Q. Xu, X. Zou, X. Lu, Mater. Today Commun. 45 (2025) 112271. 10.1016/j.mtcomm.2025.112271
[74] Sayyed M., Kaky K., and Anaee R. Chromium ions effects on Sb_2O_3-PbO-GeO_2 glass properties for radiation protection. J. Theor. Appl. Phys. 2024; 18(1). 10.57647/J.JTAP.2023.1705.55